Supporting Information

Polycyclic Aromatic Hydrocarbons as Sublimable Adhesives

*Haydn T. Mitchell,[†] Merry K. Smith,[†] Nicholas D. Blelloch,[†] Douglas W. Van Citters,[‡] and Katherine A. Mirica[†]**

[†] Burke Laboratory, Department of Chemistry, Dartmouth College, Hanover, New Hampshire 03755, United States. *Email: katherine.a.mirica@dartmouth.edu

[‡] Thayer School of Engineering, Dartmouth College, Hanover, New Hampshire 03755, United States.

(55 pages)

I. General Materials

All substrates for adhesion testing were purchased or cut to the dimensions of 75 × 25 mm. The smooth microscope glass slides (R1OH) (Gold Seal Products, Cat. #3051) and frosted microscope glass slides (R2OH) (Electron Microscopy Science, Cat. #71867-01) were both 1 mm in thickness. The plastic, poly(methyl methacrylate) (PMMA) (McMaster-Carr, #8560K171), pieces were cut to 75 × 25 × 1.5 mm pieces by a Laser Pro Spirit GLS laser cutter (GCC Innovation), with the design drawn in CorelDraw. Aluminum (Al) (6061 T6 aluminum (1.5 mm thick)) was cut to 75 × 25 × 1.5 mm using a metal shearer (Grainger Industrial, Roper Whitney Foot Squaring Shear). All materials, once cut to size, were labeled, and weighed on a balance (VWR 124B) before being bonded. The chemicals used as adhesives were naphthalene ($C_{10}H_8$) (TCI, CAS #91-20-3), 2-naphthol ($C_{10}H_7OH$) (TCI, CAS #132-19-3), 2,3-dihydroxynaphthalene ($C_{10}H_6(OH)_2$) (TCI, CAS #92-44-4), 2,3-diaminonaphthalene ($C_{10}H_6(NH_2)_2$) (TCI, CAS #771-97-1), octafluoronaphthalene ($C_{10}F_8$) (Alfa Aesar, CAS #313-72-4), anthracene ($C_{14}H_{10}$) (TCI, CAS #10387-13-0), and pyrene ($C_{16}H_{10}$) (TCI, CAS #12900-0). A common non-permanent adhesive, 3M Scotch ½" double sided tape (DST), was used for context. Trichloro(1H,1H,2H,2H-perfluoro-octyl)silane was purchased from Sigma Aldrich (CAS # 78560-45-9).

II. Modification and Measurement of Surface Features on Glass Slides

1. Silanization of Glass. Both R1OH and R2OH glass slides were silanized using trichloro(1H,1H,2H,2H-perfluoro-octyl)silane (F) by exposing the surface of glass to the vapor of the silane under reduced pressure (7 kPa) for two hours, producing silanized glass surfaces, R1F and R2F, respectively. The silanization was confirmed by measurement of the contact angle (**Figure S1**) using a contact angle goniometer (**SI Section II.2**).

2. Measurement of Contact Angle. The contact angle was measured using a contact angle goniometer (ramé-hart, Model 190-F2) for R1OH, R2OH, R1F, and R2F (**Figure S1**). A 2 μL aliquot of deionized water was dispensed onto the surface of the substrate for each contact angle measurement. Values reported are the average of left and right contact angles of three separate aliquots of 2 μL of water. This technique was also used for assessing the presence of $C_{10}H_8$ and $C_{10}F_8$ residue on glass substrates bonded and sublimed to release them (**Figure S43-44**).

3. Measurement of Surface Roughness. The surface roughness average (R_a) and surface area (SA) for each material was measured using a profilometer (Tencor, Alpha Step 200). The R_a is the average of the absolute height deviation value from the mean line determined by the profilometer.[S1] The SA was estimated using a surface area value produced by the profilometer over the length of measurement.[S1] The R_a and SA were measured over the distance of 2000 μm with the diamond tip moving at a rate of 0.2 μm s^{-1}. Seven measurements were averaged for R1OH, R1F, R2OH, R2F, Al, and PMMA to reach the reported R_a and SA values (**Table S1**).

Table S1. Surface roughness of substrates. Table with surface roughness (R_a) and surface area (SA) measurements of substrates used in experiments to assess the scope and characteristics of PAHs as nonpermanent adhesives. Values represent the average of seven measurements with standard deviation.

Substrate material	R_a	SA (μm^2)
R1OH	3 ± 1 nm	12 ± 2
R1F	3 ± 1 nm	14 ± 2
R2OH	4 ± 1 μm	8708 ± 1402
R2F	4 ± 1 μm	8846 ± 1008
Al	320 ± 70 nm	93 ± 16
PMMA	12 ± 5 nm	37 ± 19

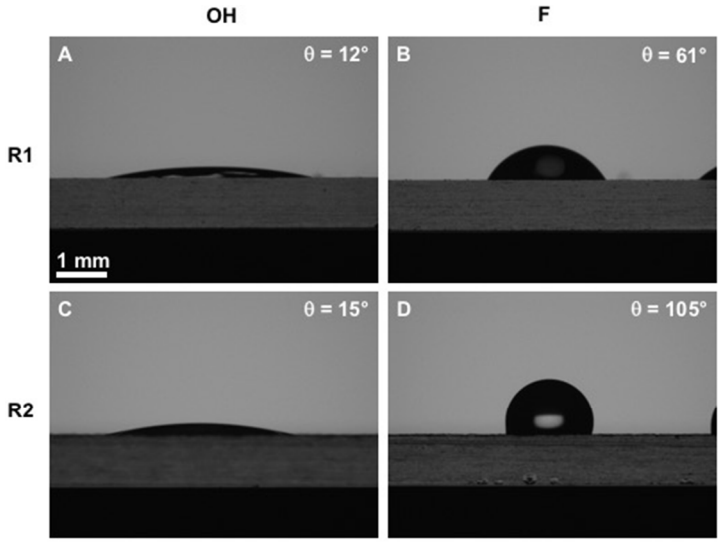

Figure S1. Contact angles (θ) of glass substrates with different surface roughness and surface chemistries using 2 μL of water. A) Image from contact angle measurement for R1OH, a hydrophilic surface. B) Image from contact angle measurement for R1F, a hydrophobic surface. C) Image from contact angle measurement for R2OH, a hydrophilic surface. D) Image from contact angle measurement for R2F, a hydrophobic surface.

III. Melt-bonding Procedures of Substrates with PAHs and Characterizing Samples

1. **General Method for Melt-bonding of Substrates with PAHs.** Substrates were bonded by heating them in a fixture made of poly(1,1,2,2-tetrafluoroethylene) (PTFE) (**Figure S2**). The PTFE apparatus was designed in E-Z Cam, and fabricated in a Proto-trak Trak DPM2. A substrate was placed within the fixture, then approximately 60 mg of PAH in the form of a solid powder was deposited on top, followed by a second, top substrate. For all PAHs the glass substrates were pressed together before melt-bonding in order to pack the crystals, reducing the mass lost from the wind of the heat gun. There was no pressure applied to the substrates while the adhesive was in a liquid phase except for the experiment described in **SI Section III.2**. The PAHs were intentionally added in excess to ensure PAH filled the overlapped area (approximately 9.4 cm^2). The remaining average mass of PAH after melt-bonding equaled 50 mg or less and is reported in **Table S2**, **S3**, **S6**, **S7**, **S8**, **S10**, and **S11** for various experiments. The differences in mass on the tens of milligrams scale had no statistically significant effect on τ (**Figure S6**).

   Of all the PAHs, $C_{10}H_8$ was the only PAH that was pulverized with a mortar and pestle prior to use. Pulverizing $C_{10}H_8$ ensured the crystals were visibly a consistent, small size to assist in uniform melting. All other PAHs were received with consistent, small crystals and thus used as received. The mesh size for these crystals was not determined, because while particle size could affect melting profile of the materials, this effect was considered negligible.

   Substrates were staggered for half of the total length of the substrates to overlap as the area to be bonded. The samples were heated using a heat gun and heating was terminated once all the mass of the adhesive had visually melted. Literature precedent showed that naphthalene and other PAHs decompose well beyond their melting points.[S2] For instance, the melting point of naphthalene is 80 °C, with a decomposition at 570 °C according to *Johns et al*.[S2] Since heating of the materials was terminated within seconds of the PAHs being visually melted, the decomposition of the PAHs is unlikely. The melt-bonded assembly was cooled at ambient conditions in the PTFE fixture, typically crystallizing within 20

seconds or less, producing a bonded area of approximately 9.4 cm^2 for each sample. Voids formed between the two glass slides (**Figure S4**) account for 2-19% of total surface area. Excess PAH spilled out at the edge of the bonded assembly; this excess was removed after cooling by scraping away with a stainless-steel razor blade. The final mass of the PAH used to bind two substrates was determined by subtracting the mass of the two pristine substrates from the mass of the melt-bonded assembly. Bonded assemblies were also prepared in an analogous manner using a hot plate rather than a heat gun. There was no statistically significant difference in τ for samples produced using a hot plate.

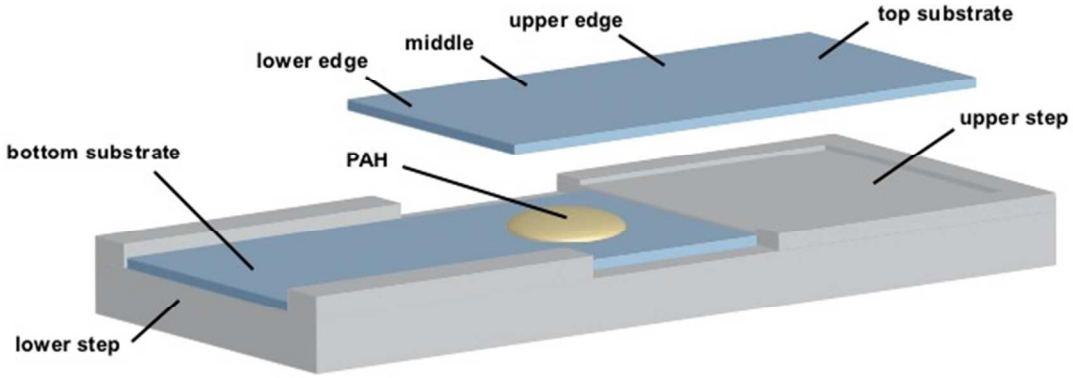

Figure S2. A depiction of the fixture used to hold substrates in place during melt-bonding. Shown are two substrates with PAH spread on the surface of substrate on the lower step. Once the top substrate is firmly fixed on top of the PAH and bottom substrate, the PAH was melted using a heat gun. The PAH was then allowed to cool, solidifying between the two substrates completing the process of melt-bonding.

2. Melt-bonding with Two Mass-Regimes of PAH. There was reason to consider the variability in the mass of PAH used to melt-bond as the cause to the variability in mechanical testing. The role of mass of PAH was tested by lap shear testing using samples with a PAH layer between 9-46 mg. A low-mass (9-20 mg) and high-mass (21-46 mg) set of samples were assembled with and without the use of pressure (100 g aluminum block, 0.98 N force), respectively. These samples were assembled by the typical method, except with the difference of application of force on top of the assembly to obtain the low-mass samples. See **Table S6** for masses and **Figure S6** for τ-values of the low-mass and high-mass samples.

3. Measuring Film Thickness of Melt-bonded Samples. The film thickness of melt-bonded assemblies was initially characterized for $C_{10}H_8$ between two glass substrates with varying surface chemistry and roughness. The film thickness of other PAHs and substrates is discussed in the next paragraph and summarized **Table S3**. The thickness and mass of each glass slide was measured using a digital display micrometer (iGaging) and analytical balance, respectively. Samples were melt-bonded following **SI Section III.1** procedure. This procedure was performed for $C_{10}H_8$ with R1OH, R2OH, R1F, and R2F. The thickness and mass for the $C_{10}H_8$-layer for all four substrate options (n = 7) were averaged and summarized in **Table S2.**

Table S2. Summary of the mean film thickness and mass for substrates melt-bonded with $C_{10}H_8$. T_a is the mean film thickness of the $C_{10}H_8$ between two substrates, based on 7 measurements. M_a is the mean mass of the $C_{10}H_8$ between two substrates, based on 7 measurements. The error in thickness and mass is the standard deviation from the mean based on n = 7 measurements.

Adhesive	Substrates	T_a (μm)	M_a (mg)
$C_{10}H_8$	R1OH/R1OH	19 ± 5	33 ± 10
	R1F/R1F	17 ± 6	23 ± 6
	R2OH/R2OH	14 ± 3	53 ± 7
	R2F/R2F	18 ± 7	44 ± 8

As part of an experiment to assess the effect of surface chemistry on the mechanism of failure (**SI Section VIII**), the film thickness of the PAH layer between various R1-substrates was characterized more rigorously than seen in **Table S2**. An artifact of the melt-bonding method (**SI Section III.1**) was observed during this experiment (**SI Section VIII**): the glass substrates exhibit a small tilt over the melt-bonded area. **Figure S3** is an exaggerated depiction of the tilt between substrates. The film thickness was measured in three regions of the assembly, the lower edge (LE), middle (M), and upper edge (UE) (**Figure S3**). The average film thickness for LE, M, and UE for all four PAHs ($C_{10}H_8$, $C_{10}F_8$, $C_{10}H_6(OH)_2$, and $C_{10}H_6(NH_2)_2$) between various R1-substrate combinations (OH/OH, OH/F, F/F) was 26 ± 6, 37 ± 9, and 61 ± 13 μm thick, respectively (**Table S3**). The total M-value in **Table S3**, 37 ± 9 μm, is considered an average film thickness representative for any assembly bonded by the melt-bonding procedure reported in **SI Section III.1**. The angle of the tilt between substrates was calculated using **Equation 1**.[S3] The mean tilt for all substrates was 0.00097 ± 0.00048°, and it considered to have negligible influence on the lap shear testing. These averages are based on $8 \leq n \leq 10$.

Equation S1 is a geometric identity of a triangle used in this case to solve for the angle (α) of the tilt between two glass slides melt-bonded together. Taking the inverse tangent (arctan) of the opposite side (y) divided by the adjacent side of the triangle (x) calculates the angle (α) between the sides.[S3] Typically, LE thickness was lower than UE thickness, but there are a few cases in which the LE thickness was greater than UE thickness. In this case the angle of tilt was calculated to be negative rather than positive. The angle calculated would not significantly affect the accuracy of the lap shear testing (**SI Section V**).

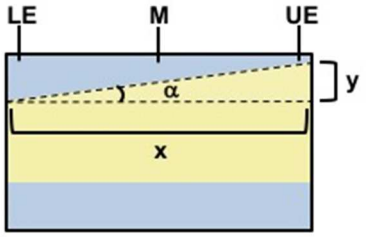

Figure S3. A depiction, not drawn to scale, of a small artifact in the tilt between two melt-bonded substrates. The thickness of the lower edge (LE), middle (M), and upper edge (UE) of the overlapped, melt-bonded area were measured. The angle (α) of the tilt between two glass slides melt-bonded together was determined by calculating the inverse tangent of the opposite side (y) divided by the adjacent side of the triangle (x) (**Equation S1**).[S3] Although the difference in film thickness between LE and UE is measurable, the micrometer scale difference in film thickness between the LE and UE is negligible over x (= 3.5 cm).

$$\boldsymbol{arctan\left(\frac{y}{x}\right) = \alpha} \qquad \textbf{(S1)}$$

Table S3. Summary of the thickness at three different locations and angle of tilt of various substrate, PAH melt-bonded assemblies. The average thickness of the lower edge (LE), middle (M), upper edge (UE) (**Figure S3**), mass (M_a) and τ-values are summarized. The error for these averages are the standard deviation ($8 \leq n \leq 10$). The bottom row is the average of all the averages from the various adhesives and substrate combinations. The error for these "Average for all samples" is the propagated error from the standard deviations of the values for each adhesive and substrate combination.

Adhesive	Substrates	LE (μm)	M (μm)	UE (μm)	M_a (mg)	τ (N cm^{-2})
$C_{10}H_8$	OH/OH	19 ± 4	54 ± 15	86 ± 22	42 ± 15	20 ± 3
$C_{10}H_8$	OH/F	25 ± 9	39 ± 13	62 ± 28	38 ± 9	11 ± 3
$C_{10}H_8$	F/F	28 ± 12	49 ± 22	72 ± 41	41 ± 11	16 ± 4
$C_{10}F_8$	OH/OH	24 ± 9	32 ± 6	48 ± 12	52 ± 13	15 ± 3
$C_{10}F_8$	OH/F	40 ± 42	30 ± 9	39 ± 10	52 ± 9	10 ± 4
$C_{10}F_8$	F/F	27 ± 18	38 ± 9	56 ± 16	54 ± 9	10 ± 4
$C_{10}H_6(NH_2)_2$	OH/OH	32 ± 23	34 ± 9	60 ± 11	33 ± 10	16 ± 4
$C_{10}H_6(OH)_2$	OH/OH	24 ± 9	30 ± 9	59 ± 11	38 ± 7	30 ± 3
$C_{10}H_6(OH)_2$	OH/F	23 ± 9	32 ± 5	66 ± 7	42 ± 6	16 ± 2
$C_{10}H_6(OH)_2$	F/F	18 ± 7	30 ± 8	66 ± 13	32 ± 6	13 ± 3
Average of all samples		26 ± 6	37 ± 9	61 ± 13	42 ± 3	16 ± 6

The film thickness of the PAH layer for melt-bonded samples was not measured for all assemblies. In these cases, the film thickness was estimated (T_e, μm) based on the average mass (M_a) of the assemblies (see **Tables S6-8**). Dividing M_a by the density (mg cm^{-3}) of the PAH, then multiplying by the surface area of the adhesive between the two substrates (cm^2), and converting from centimeters to micrometers (10^3 μm cm^{-1}) estimates the T_e (μm). To simplify the estimation, the surface area for all samples was assumed to be 9.0 cm^2, since the surface area of PAH was unquantifiable for the Al to Al, Al to R1OH, and Al to PMMA assemblies melt-bonded with $C_{10}H_8$ (**Figure S7**). The film thickness was estimated for these samples to judge whether their film thicknesses deviated substantially from the reported film thickness average of 37 ± 9 μm. Many of the estimated film thicknesses are within a standard deviation of the reported average film thickness (see **Table S6-8**). The density of $C_{10}H_8$, $C_{10}F_8$, $C_{10}H_6(OH)_2$, $C_{10}H_6(NH_2)_2$, $C_{14}H_{10}$, and $C_{16}H_{10}$ is 1.14, 1.73, 1.12, 1.10, 1.25, and 1.27 g cm^{-3}, respectively.[S4]

IV. Method of Capturing and Analyzing Optical Micrographs to Measure Adhered-Surface Area

1. Capturing Optical Micrographs of Adhered Surfaces. All samples were imaged using a Keyence High Definition Light Microscope prior to lap shear testing (**SI Section V**) except assemblies with a metal substrate. An auxiliary light source was used to direct light at approximately a 15° angle above the horizontal plane of the sample, causing more light scattering with the desired effect of greater contrast between the areas of PAH and voids. For dark areas of the optical images in **Figure S4**, there is either a void or the PAH is transparent. The solid-state structures of the PAH were not visible for the aluminum/aluminum samples due to lack of one transparent substrate. For these samples, the surface area of the adhesive was assumed to be 90% of the total overlap surface area. Darkly tinted glass was used as a background to dampen reflecting light, which improved relief of the crystal features. For R2-substrates, there was difficulty viewing the PAHs as clearly as with R1-substrates since the surface roughness caused scattering, and reduced accuracy of measuring surface area of PAH between the surfaces.

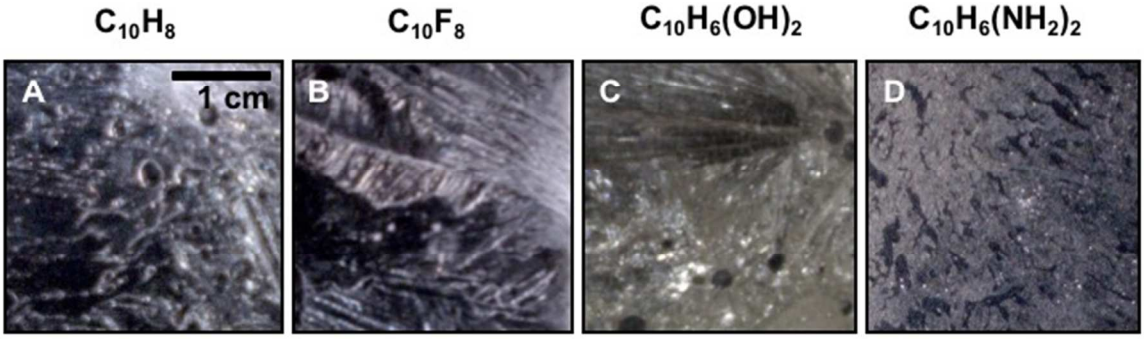

Figure S4. Optical images of R1OH/R1OH bonded by various PAHs with voids and crystalline features. A) An optical image of $C_{10}H_8$ between R1OH substrates. B) An optical image of $C_{10}F_8$ between R1OH substrates. C) An optical image of $C_{10}H_8(OH)_2$ between R1OH substrates. D) An optical image of $C_{10}H_8(NH_2)_2$ between R1OH substrates. These samples were a part of a sample set of 10 samples; the τ-values of the sample set are in **Figure 2a** and **Figure S6**. Thickness of the adhesive layer for these samples was not measured, refer to LM T_e in **Table S6** for an estimated film thickness.

2. Analysis of Optical Micrographs of PAHs Between Glass Slides. Surface area of PAH between substrates was measured by processing the optical micrographs in ImageJ 5.0. The scale was set within the image. The Threshold plugin allowed for the contrast between the light reflecting and transparent regions, areas with adhesive and without adhesive (voids), respectively, to be maximized. The image was converted to an 8-bit image type. The image was adjusted to display the light regions as red and the dark regions as black. A quadrilateral was drawn to enclose the total surface area of the substrate overlap-area. The total surface area and adhered area were measured using the Measure and Analyze Particles functions, respectively. The measured surface area of the adhesive between substrates was used to calculate the τ-value for each sample. The percent surface area of voids was calculated by subtracting the value of surface area of PAH between substrates from the value of total surface area of the overlap joint and dividing by the total surface area of the overlap joint.

V. Lap Shear Testing

We employed a lap shear testing protocol similar to ASTM D-1002-10[S5] to quantify the maximum force required to separate two substrates bonded by a PAH. Lap shear testing was performed using an Instron 5544 at a loading rate of 30 N min^{-1}. Results were recorded with Blue Hill software and analyzed in Microsoft Excel. **Figure S5** is a typical load versus extension profile for lap shear testing of these crystalline materials. To account for small variations in adhered surface area, we introduced the parameter τ (N

cm^{-2}) as the ratio of the maximum load (N) before the joint failed, to the surface area (cm^2) covered by the adhesive (**Equation S2**).[S6] Ten samples were prepared for each set of conditions, but depending on the lap shear strength only some were measured accurately (**Figure S8**).

$$\tau = \frac{maxium\ load}{surface\ area\ of\ adhesive} \quad \textbf{(S2)}$$

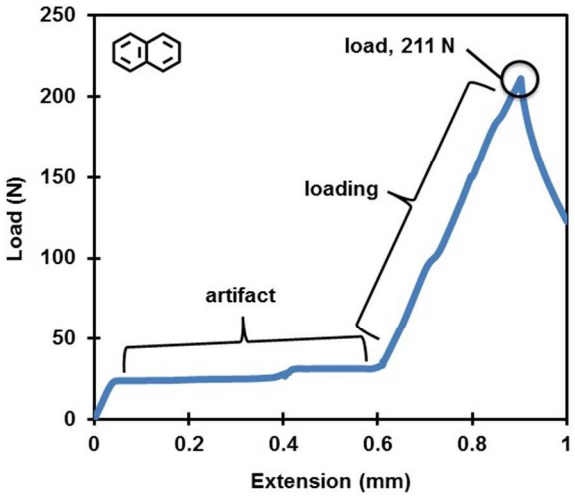

Figure S5. A representative graph of the raw data from a lap shear test for $C_{10}H_8$ between two R1OH substrates. The profile includes three major segments; "artifact", "loading", and "load". The clamps are stretching out during the artifact segment. Once the clamps have settled into their final grip position, the mechanical tester is able to start "loading" the sample. The R1OH substrates bonded with $C_{10}H_8$ are being loaded without deforming during the inelastic "loading" segment. The maximum load value is labeled as the "load". The "load" is used as the value to represent that sample's strength and used to calculate τ.

As addressed in the main text, for some PAH/surface combinations the strength of the PAH/surface adhesion and PAH/PAH cohesion are so strong it causes mechanical failure of the glass slides during lap shear testing. This observation is reasonable considering a 1 cm thick piece of commercial glass has a mechanical strength of 2,000-4,000 N cm^{-2}, depending on the quality.[S7] The glass slides have a cross sectional area perpendicular to the direction of load of 0.25 cm^2. This cross-sectional area could withstand 500-1000 N, depending on the quality of glass. Some of the measured load values for assemblies (glass bonded to glass with PAH) in this study resulted in the glass substrate failing at a load value as high as 450 N. A possible cause for the glass failing prematurely may be the misalignment of the substrates while under load, as described in **SI Section III.3**.

VI. Melt-bonding with a Range of PAHs

The general procedure for bonding R1OH with R1OH surfaces was performed for the following adhesives: $C_{10}H_8$, $C_{10}H_7OH$, $C_{10}H_6(OH)_2$, $C_{10}H_6(NH_2)_2$, $C_{10}F_8$, $C_{14}H_{10}$, and $C_{16}H_{10}$. The adhesive control was double sided tape (DST). The bond-strength of the PAHs varied (**Figure 2a** and **Figure S6**). This led to three distinct mechanisms of failure of the joint between bonded substrates: 1) the joint could not withstand typical handling to reach lap shear testing, a premature failure (PF), 2) the adhesives failed during lap shear testing, an adhesive failure (AF), 3) and the substrate failed during lap shear testing, a substrate failure (SF). In this case, AF does not distinguish between failure at the PAH/surface interface and within the PAH bulk and is used to describe either or both mechanical failure possibilities. These mechanisms of failure will be described as such for rest of the Supporting Information. Two strips of DST were measured and cut to cover half of the surface area of a glass slide or substrate. The tape was pressed to one slide, the second slide was pressed onto that taped-face and then a final press was performed using a book. Additionally, samples of two mass regimes were tested for $C_{10}H_8$, $C_{10}H_6(OH)_2$, $C_{10}H_6(NH_2)_2$, $C_{10}F_8$, $C_{14}H_{10}$, and $C_{16}H_{10}$. The details on the mechanism of failure for each PAH are provided in **Tables S4-5** for the high- and low-mass regimes, respectively. **Table S6** shows the average mass for the high- and low-mass regimes, respectively. Lap shear results for high- and low-mass regimes for R1OH/R1OH are plotted in **Figure S6**.

Table S4. Summary of the mechanism of failure for the samples used for the high-mass regimes samples in Figure S6. Column PF is the number of samples for which the adhesive failed prior to testing. Column AF is the number of samples that were tested and failed at the adhesive-substrate interface. Column SF is the number of samples for which the substrate failed during testing. Ten samples were made for all adhesives. Thickness of the adhesive layer for these samples was not measured.

Adhesive	PF	AF	SF
$C_{10}H_8$	0	10	0
$C_{10}H_7OH$	0	10	0
$C_{10}H_6(OH)_2$	0	10	0
$C_{10}H_6(NH_2)_2$	7	3	0
$C_{10}F_8$	0	10	0
$C_{14}H_{10}$	0	10	0
$C_{16}H_{10}$	0	10	0

Table S5. Summary of the mechanism of failure for the samples used for the low-mass regimes samples in Figure S6. Column PF is the number of samples for which the adhesive failed prior to testing. Column AF is the number of samples that were tested and failed at the adhesive-substrate interface. Column SF is the number of samples for which the substrate failed during testing. Ten samples were made for all adhesives. Thickness of the adhesive layer for these samples was not measured.

Adhesive	PF	AF	SF
$C_{10}H_8$	0	10	0
$C_{10}H_6(OH)_2$	0	10	0
$C_{10}H_6(NH_2)_2$	4	6	0
$C_{10}F_8$	0	10	0
$C_{14}H_{10}$	0	10	0
$C_{16}H_{10}$	0	10	0

Table S6. Two regimes of mass for PAHs being used as adhesives. The mean final mass of adhesive for all R1OH/R1OH samples in **Figure S6**. M_a corresponds to the mean of the PAH's mass for 10 measurements for two different experimental procedures. The error represents the standard deviation for n = 10 measurements. Each sample was made starting with ~60 mg of PAH. Thickness of the adhesive layer for these samples was not measured. T_e is an estimation of the adhesive layer thickness; calculated using the recorded mass and density of PAH. Thickness of the adhesive layer for the high-mass (HM T_e) and low-mass (LM T_e) samples were estimated. The error is then propagated standard deviation from the mass for the respective samples. The surface area was assumed to be 10 cm^2 for each sample.

Adhesive	High M_a (mg)	HM T_e (μm)	Low M_a (mg)	LM T_e (μm)
$C_{10}H_8$	37 ± 10	36 ± 10	9 ± 5	9 ± 5
$C_{10}H_6(OH)_2$	45 ± 17	45 ± 17	11 ± 5	11 ± 5
$C_{10}H_6(NH_2)_2$	30 ± 10	30 ± 10	17 ± 3	17 ± 3
$C_{10}F_8$	44 ± 16	28 ± 10	17 ± 3	11 ± 2
$C_{14}H_{10}$	41 ± 9	36 ± 8	37 ± 4	33 ± 4
$C_{16}H_{10}$	46 ± 13	40 ± 11	39 ± 5	34 ± 4

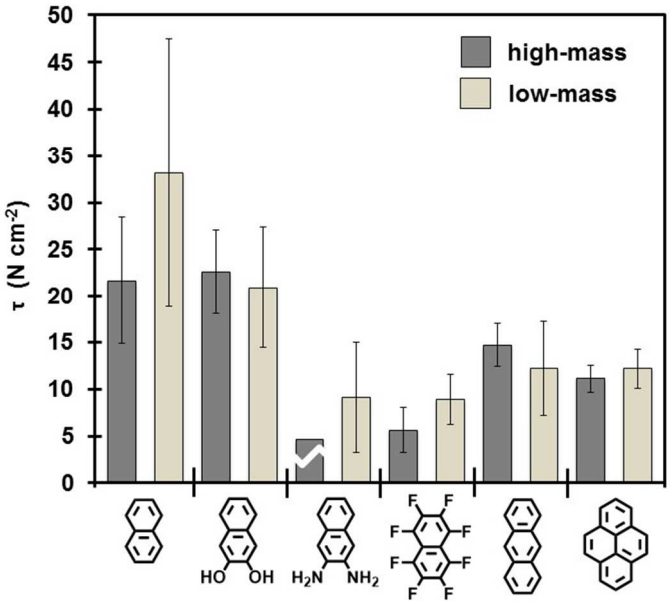

Figure S6. Lap shear testing of glass slides melt-bonded with six PAHs have a low-mass (9-20 mg) and high-mass (21-46 mg) regime layer, with little to no effect on the τ-values. The τ-values for low-mass and high-mass regimes for $C_{10}H_8$, $C_{10}H_6(OH)_2$, $C_{10}H_6(NH_2)_2$, $C_{10}F_8$, $C_{14}H_{10}$, and $C_{16}H_{10}$ are represented by columns ($n \geq 5$) and errors bars represent the standard deviation. A single line breaking the column indicates a majority of the samples failed before reaching the mechanical tester ($n < 5$). The estimated film thickness of these assemblies are reported in **Table S6**.

VII. Melt-bonding Various Substrates Using PAHs

Encouraged by the success of PAHs as adhesives with glass substrates, we tested the generality of PAHs as adhesives by melt-bonding a variety of surfaces together. Naphthalene is capable of bonding Al to Al, Al to R1OH, and Al to PMMA with τ-values of 19 ± 5 N cm^{-2}, 12 ± 5 N cm^{-2}, and 52 ± 22 N cm^{-2}, respectively (**Figure S7**). The average mass and estimated film thickness for each assembly is summarized in **Table S7**. The large τ accompanied by a large error for bonding aluminum to PMMA is likely due to heating the PMMA past its glass transition temperature (T_g), causing the polymer to soften and flow into the surface features of the Al.[S8] Subsequent cooling of PMMA to a temperature below its T_g would cause hardening of the polymer, accompanied by intercalation of naphthalene into the polymer strands, thereby promoting structural rigidity. PMMA has been known to be used as an adhesive.[S8]

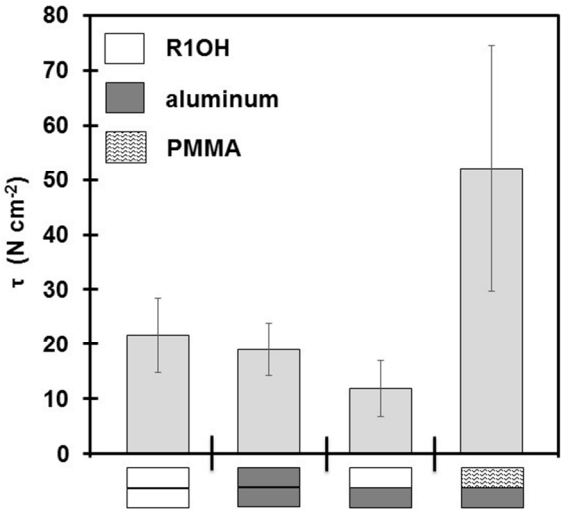

Figure S7. Plot of τ for various materials melt-bonded with $C_{10}H_8$. Columns represent the average of seven or more measurements. The error bars represent the standard deviation for $n \geq 7$ measurements. Thickness of the adhesive layer for these samples was not measured. See **Table S7** for estimates of film thickness (T_e).

Table S7. The mean final mass of melt-bonding R1OH/R1OH, Al/Al, Al/R1OH, and Al/PMMA with $C_{10}H_8$. M_a corresponds to the mean mass of the adhesive, based on the 10 measurements for the samples in **Figure S7**. The error in mass is the standard deviation from the mean based on n = 10 measurements. Thickness of the adhesive layer for these samples was not measured. T_e is an estimation of the adhesive layer thickness; calculated using the recorded mass and density of PAH. The error is the propagated

standard deviation from the mass for the respective samples. The surface area was assumed to be 10 cm^2 for each sample.

Adhesive	Substrates	M_a (mg)	T_e (μm)
$C_{10}H_8$	R1OH/R1OH	37 ± 10	36 ± 10
	Al/Al	36 ± 11	35 ± 11
	Al/R1OH	35 ± 8	34 ± 8
	Al/PMMA	36 ± 7	35 ± 7

Additional experiments were performed using various glass substrates R1F/R1F, R1OH/R2OH, R1F/R2F, R2OH/R2OH, and R2F/R2F with the following PAHs: $C_{10}H_8$, $C_{10}H_6(OH)_2$, $C_{10}H_6(NH_2)_2$, and $C_{10}F_8$. Reference **Table S8** for the average mass and estimated film thickness of the PAH for each set of assemblies, including the R1OH/R1OH assemblies. Refer to **Table S9** for an account on the mechanism of failure for each PAH, substrate combination. See **Figure S8** for the plotting of the τ-values.

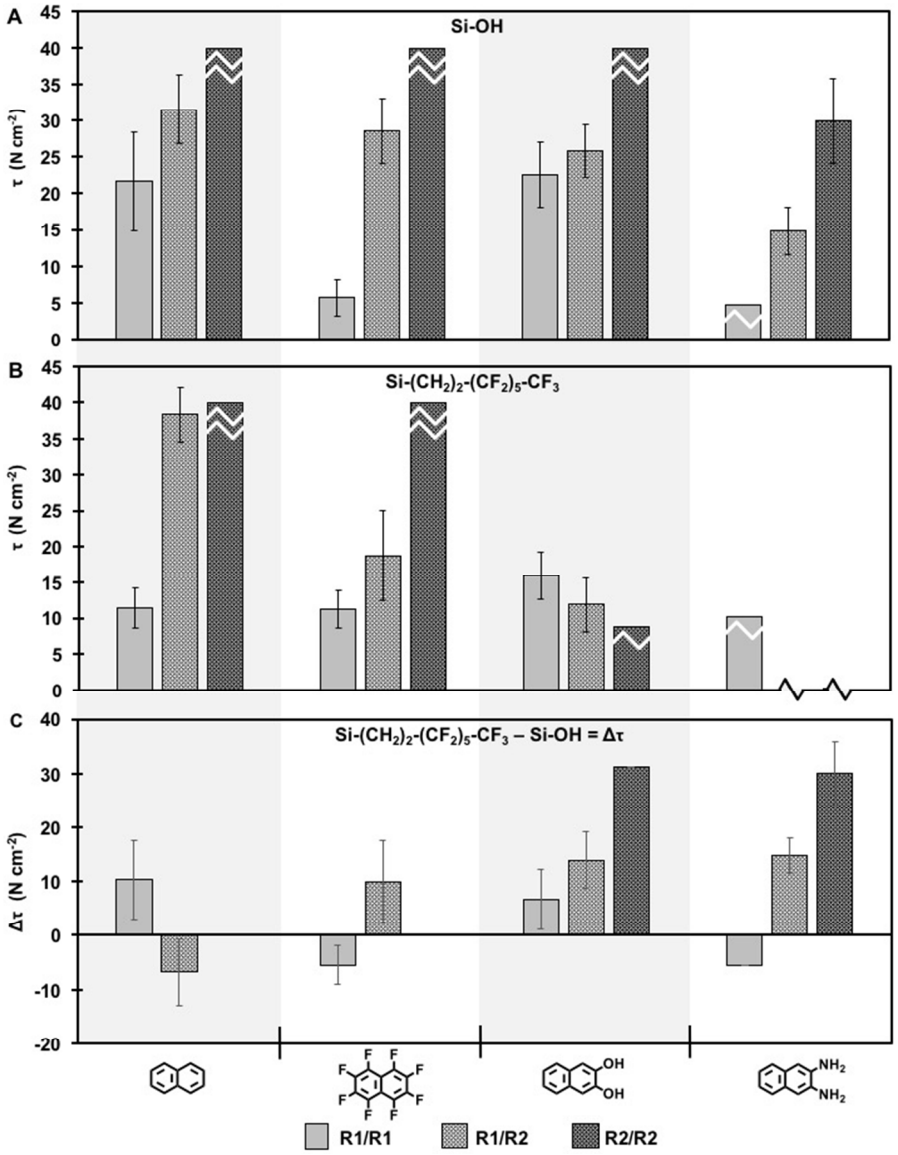

Figure S8. The τ-values for $C_{10}H_8$, $C_{10}F_8$, $C_{10}H_6(OH)_2$, and $C_{10}H_6(NH_2)_2$ on a combination of R1OH, R1F, R2OH, and R2F demonstrating the contribution of surface chemistry and roughness on τ. A) The τ-values for $C_{10}H_8$, $C_{10}F_8$, $C_{10}H_6(OH)_2$, and $C_{10}H_6(NH_2)_2$ on surfaces with increasing surface roughness. Each bar represents the mean τ-value of $n \geq 5$ with the error bars representing the standard deviation. Single-line breaks represent > 5 samples out of 10 samples failed before mechanical testing. Double-line breaks represent when substrates of > 5 samples out of 10 samples broke during mechanical testing. For these sets of samples the τ-value was set to 40 N cm^{-1} as a representative value. B) The τ-values for $C_{10}H_8$, $C_{10}F_8$, $C_{10}H_6(OH)_2$, and $C_{10}H_6(NH_2)_2$ on surfaces with increasing surface roughness. C) The $\Delta\tau$ represents the difference for $C_{10}H_8$, $C_{10}F_8$, $C_{10}H_6(OH)_2$, and $C_{10}H_6(NH_2)_2$ on surfaces with OH and F surface chemistry with varying surface roughness. Thickness of the adhesive layer for these samples was not measured. T_e is an estimation of the adhesive layer thickness; calculated using the recorded mass and density of PAH (**Table S8**). The error is the propagated standard deviation from the mass for the respective samples. The surface area was assumed to be 10 cm^2 for each sample.

Table S8. The mean mass for all PAH/substrate combinations. The mean mass of adhesive for compounds used with R1OH, R1F, R2OH, and R2F combinations in **Figure S8**. M_a corresponds to the mean mass of the adhesive, based on 10 measurements. The error in mass in the standard deviation from the mean based on n = 10 measurements. Thickness of the adhesive layer for these samples was not measured. T_e is an estimation of the adhesive layer thickness; calculated using the recorded mass and density of PAH. The error is the propagated standard deviation from the mass for the respective samples.

Adhesive	Substrate	M_a (mg)	T_e (μm)
$C_{10}H_8$	**R1OH/R1OH**	37 ± 10	36 ± 10
	R1F/R1F	29 ± 21	28 ± 20
	R1OH/R2OH	28 ± 8	27 ± 8
	R1F/R2F	55 ± 15	54 ± 15
	R2OH/R2OH	29 ± 5	28 ± 5
	R2F/R2F	39 ± 8	38 ± 8
$C_{10}H_6(OH)_2$	**R1OH/R1OH**	45 ± 17	45 ± 17
	R1F/R1F	26 ± 11	26 ± 11
	R1OH/R2OH	42 ± 13	42 ± 13
	R1F/R2F	46 ± 19	46 ± 19
	R2OH/R2OH	29 ± 5	29 ± 5
	R2F/R2F	35 ± 11	35 ± 11
$C_{10}H_6(NH_2)_2$	**R1OH/R1OH**	26 ± 6	26 ± 6
	R1F/R1F	35 ± 10	35 ± 10
	R1OH/R2OH	33 ± 6	33 ± 6
	R1F/R2F	NA	NA
	R2OH/R2OH	37 ± 12	37 ± 12
	R2F/R2F	NA	NA
$C_{10}F_8$	**R1OH/R1OH**	44 ± 16	28 ± 10
	R1F/R1F	29 ± 7	19 ± 4
	R1OH/R2OH	41 ± 11	26 ± 7
	R1F/R2F	51 ± 20	33 ± 13
	R2OH/R2OH	32 ± 4	21 ± 3
	R2F/R2F	41 ± 13	26 ± 8

Table S9. Summary of the mechanism of failure for various PAH/substrate combinations. Column PF (premature failure) is the number of assemblies for which the adhesive failed prior to testing for assemblies in **Figure S8**. Column AF (adhesive failure) is the number of samples that were tested and failed at either PAH/surface or PAH/PAH interface. Column SF (substrate failure) is the number of samples for which the substrate failed during testing. Ten samples were made for all adhesive and substrate iterations.

Adhesive	Substrate	PF	AF	SF
$C_{10}H_8$	**R1OH/R1OH**	0	10	0
	R1F/R1F	0	10	0
	R1OH/R2OH	0	5	5
	R1F/R2F	0	7	3
	R2OH/R2OH	0	0	10
	R2F/R2F	0	3	10
$C_{10}H_6(OH)_2$	**R1OH/R1OH**	0	10	0
	R1F/R1F	0	10	0
	R1OH/R2OH	0	9	1
	R1F/R2F	1	9	0
	R2OH/R2OH	0	0	10
	R2F/R2F	10	0	0
$C_{10}H_6(NH_2)_2$	**R1OH/R1OH**	7	3	0
	R1F/R1F	7	3	0
	R1OH/R2OH	1	9	0
	R1F/R2F	10	0	0
	R2OH/R2OH	0	10	0
	R2F/R2F	10	0	0
$C_{10}F_8$	**R1OH/R1OH**	0	10	0
	R1F/R1F	0	10	0
	R1OH/R2OH	0	9	1
	R1F/R2F	0	9	1
	R2OH/R2OH	0	0	10
	R2F/R2F	0	1	9

VIII. Assessing the Effect of Surface Chemistry on the Mechanism of Failure

Samples consisted of two glass slides of similar (OH/OH and F/F) or dissimilar (OH/F) surface chemistry bonded with a PAH. All glass slides had average surface roughness (R_a) of 3 ± 1 nm. The surface chemistry was switched from OH to F functionality by the procedure described in **SI Section II.3**. Samples were melt-bonded and sheared according to the procedures described in **SI Section III** and **V**, respectively. The mass, film thickness, adhered-surface area, and max load withstood of the assembly were measured following typical protocols (**SI Section III**, **IV**, and **V**). The adhered-surface area and max load were used to calculate τ, plotted in **Figure S9**. Optical micrographs of each assembly and the two separated substrates after lap shear testing are organized in **Figure S10-19**. In addition to optical micrographs, the mass of PAH remaining on each substrate after lap shear testing was measured. To further assess the mechanism of failure of the PAH fractures at the PAH/surface interface, infrared spectroscopy (IR) was

used to assess the presence of PAHs on either of the two adhered-surfaces for one assembly from each set of PAH and surface chemistry conditions (**Figure S20-23**). Spectra were recorded using 16 scans at locations in which the PAH was either optically visible or not visible to assess the cleanliness of the PAH/surface interface fracture. Measurements were taken using a JASCO FT/IR-6200, operated through Jasco's Spectra Manager Version 2 (Version 2.10.01 [Build 1]). A characteristic IR spectrum for a PAH was observed clearly for locations measured with visible PAH crystals and not observed for locations without visible PAH. These spectra assist in determining whether the assembly failed by cohesive (leaving PAH on both sides) or adhesive failure (the PAH resides solely on one surface) with consideration of the detection limit of the IR instrument. The IR instrument has a detection limit that requires the material be ~5 nm thick. The mass of PAH, film thickness at LE, M, and UE (**Figure S3**), load, τ, and mass of PAH on the top and bottom surfaces are summarized in **Table S10**.

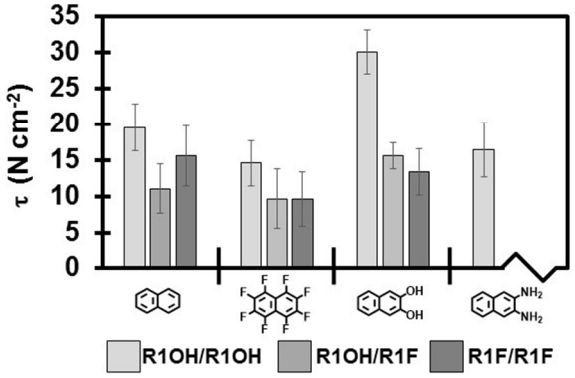

Figure S9. The effect of surface chemistry on τ-values determined for a combination of R1OH and R1F substrates for four PAHs. The bars represent the mean ($8 \leq n \leq 10$) and the error bars are the standard deviation from this mean value. The thicknesses of these samples are reported in **Table S3**.

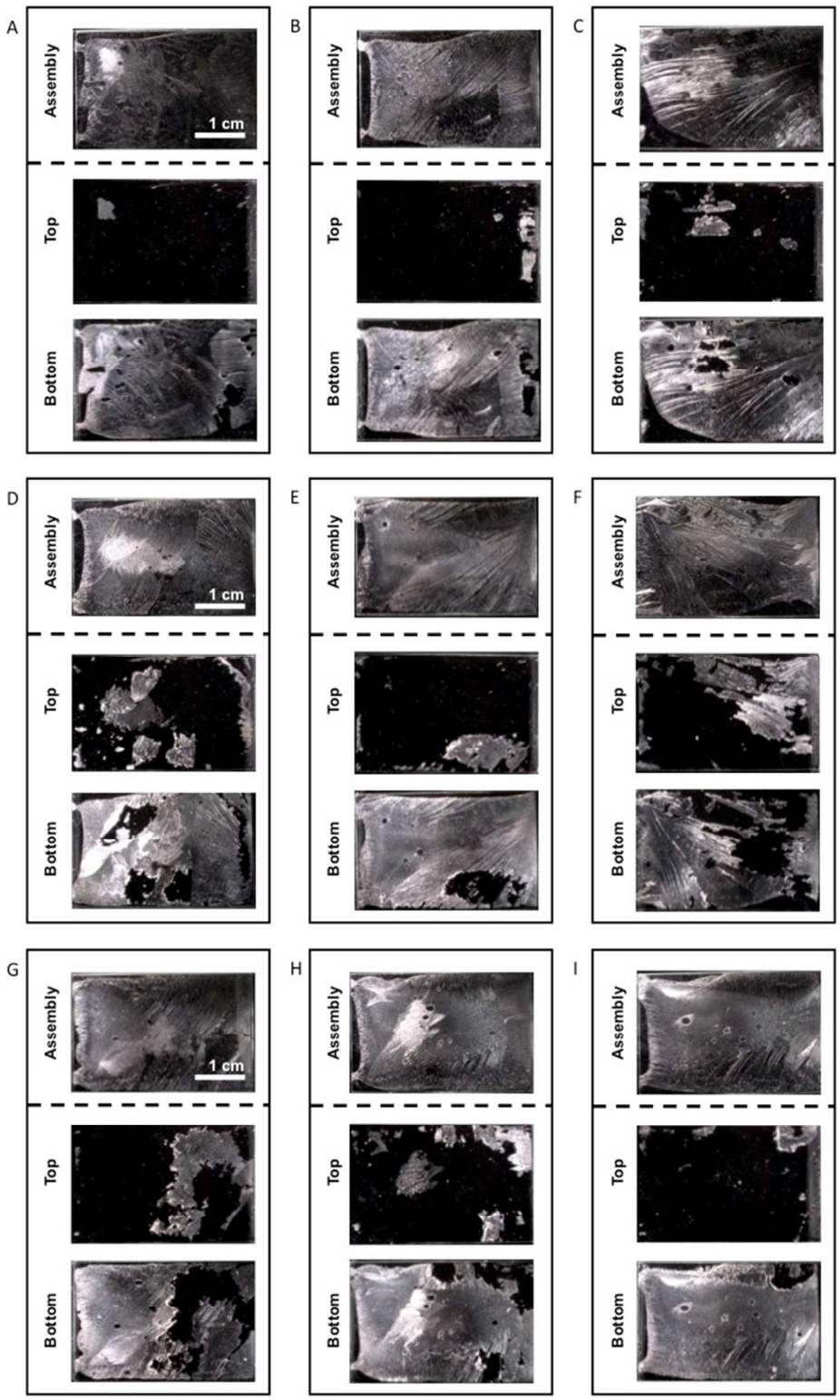

Figure S10. Optical micrographs of $C_{10}H_8$ R1OH/R1OH samples before (Assembly) and after (Top, Bottom) lap shearing. A, I) Sample exhibits primarily adhesive failure. B-C, G-H) Samples exhibit primarily adhesive failure with cohesive failure along grain boundaries. D-F) Samples exhibit both adhesive failure and cohesive failure along grain boundaries.

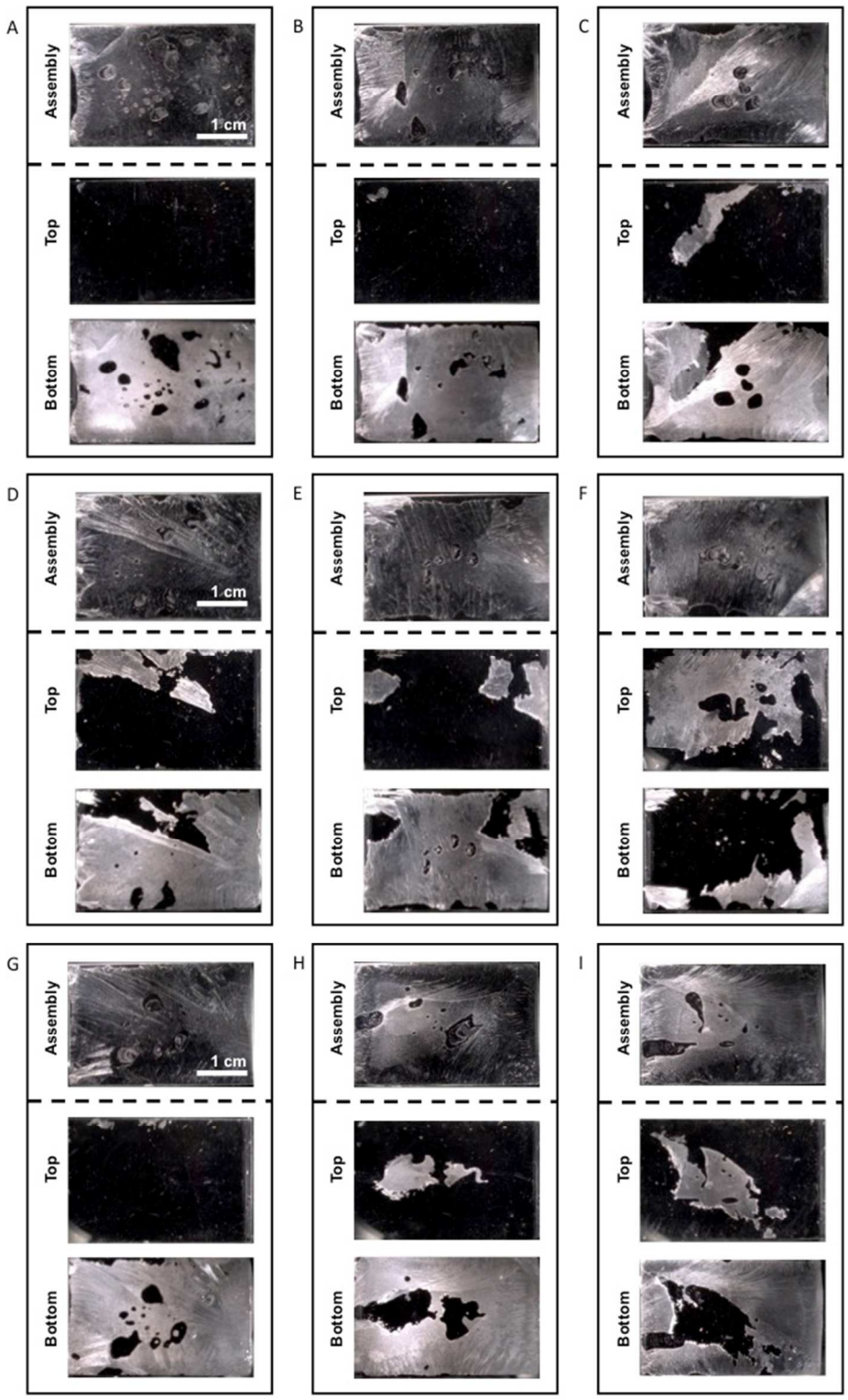

Figure S11. Optical micrographs of $C_{10}H_8$ R1OH/R1F samples before (Assembly) and after (Top, Bottom) lap shearing. A-B, G) Samples exhibit primarily adhesive failure. C-F) Sample exhibits primarily adhesive failure with cohesive failure along the grain boundaries. H-I) Sample exhibits both adhesive failure and cohesive failure along the grain boundaries.

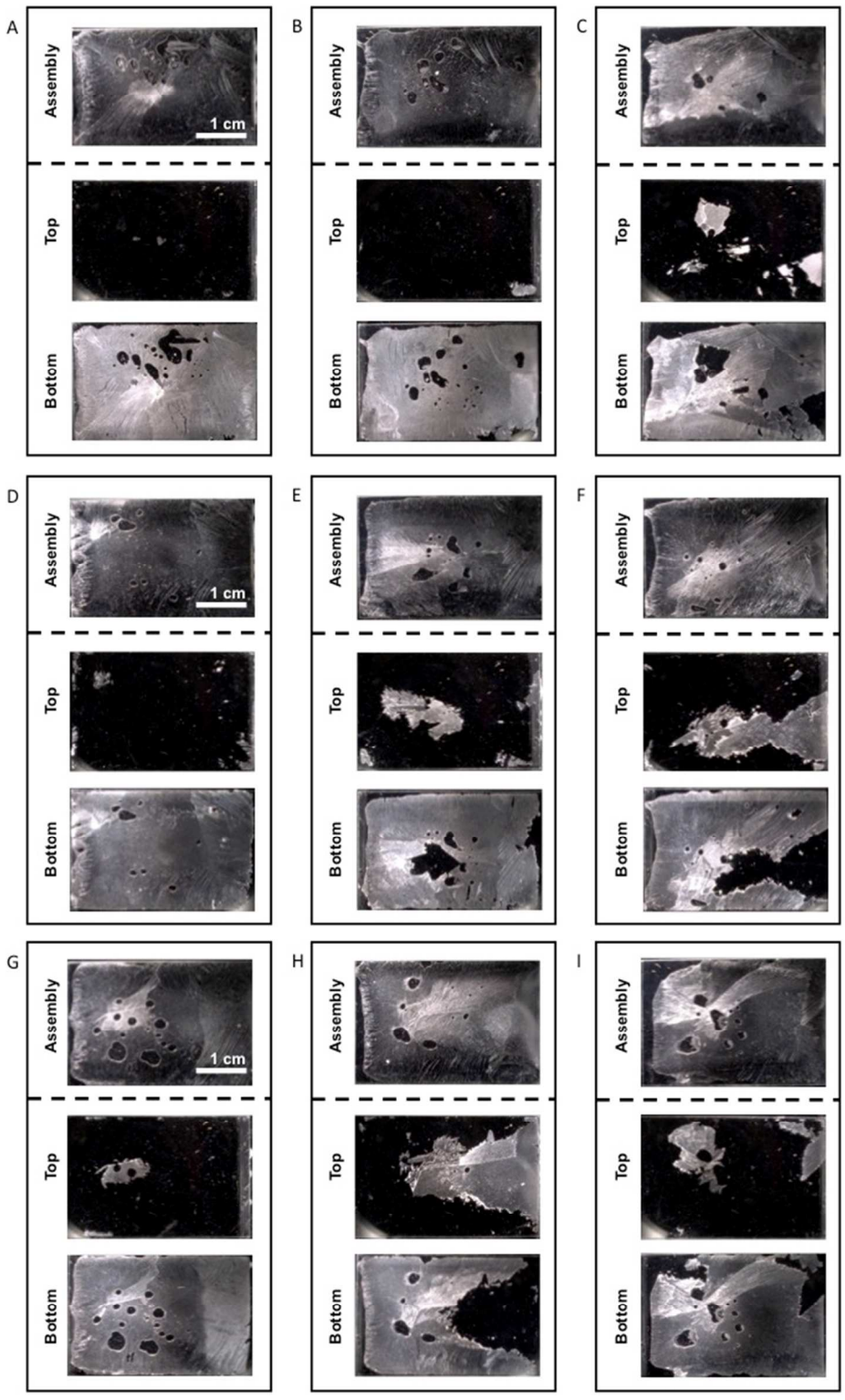

Figure S12. Optical micrographs images of $C_{10}H_8$ R1F/R1F samples before (Assembly) and after (Top, Bottom) lap shearing. A-B, D) Samples exhibit primarily adhesive failure. C, G, I) Sample exhibits primarily adhesive failure with cohesive failure along the grain boundaries. E-F, H) Samples exhibit both adhesive failure and cohesive failure along the grain boundaries.

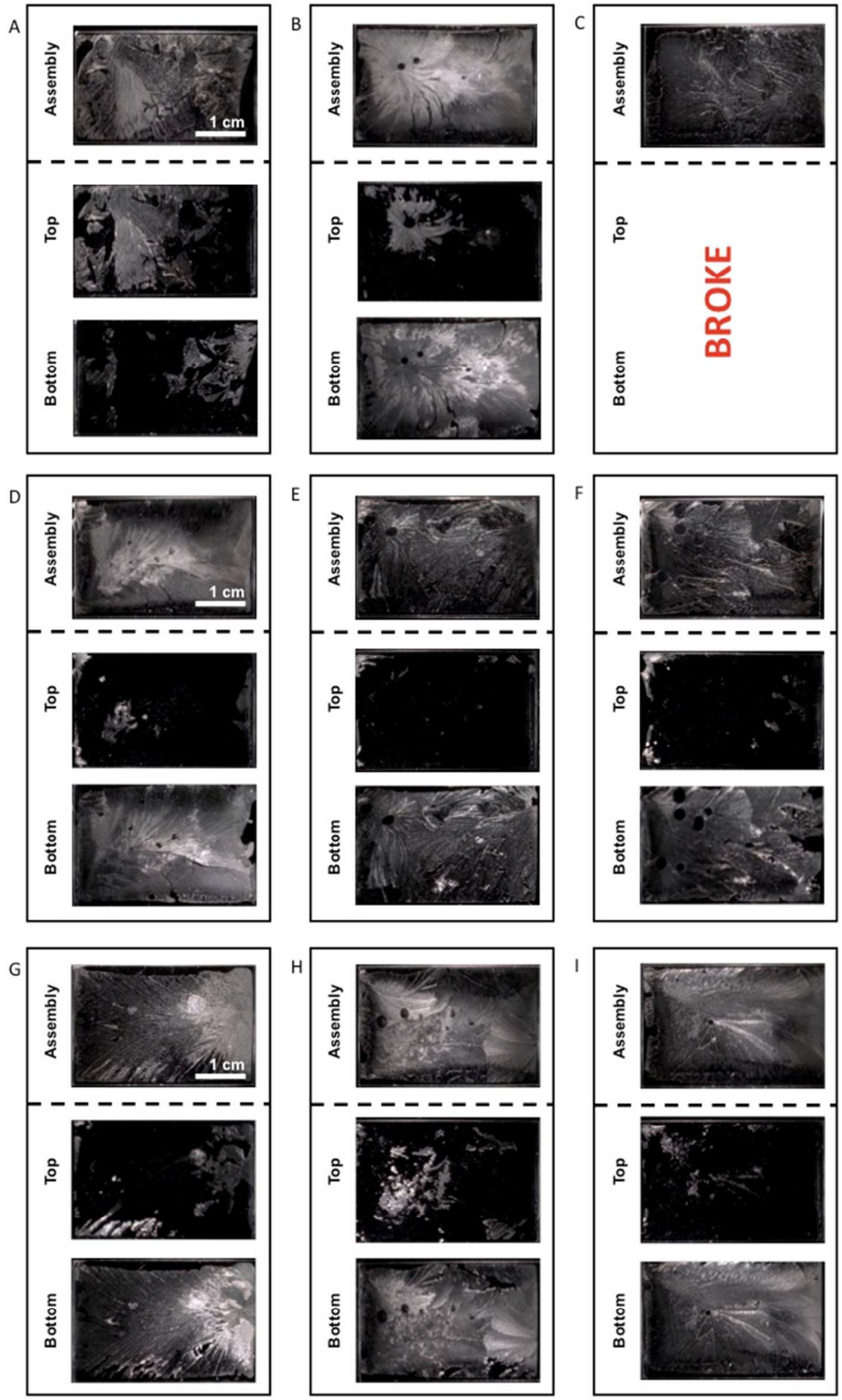

Figure S13. Optical micrographs of $C_{10}F_8$ R1OH/R1OH samples before (Assembly) and after (Top, Bottom) lap shearing. A-B) Samples exhibit both adhesive failure and cohesive failure along grain boundaries. C) Sample sheared prior to mechanical testing. D-F) Samples exhibit primarily adhesive failure. G-I) Samples exhibit primarily adhesive failure with cohesive failure along grain boundaries.

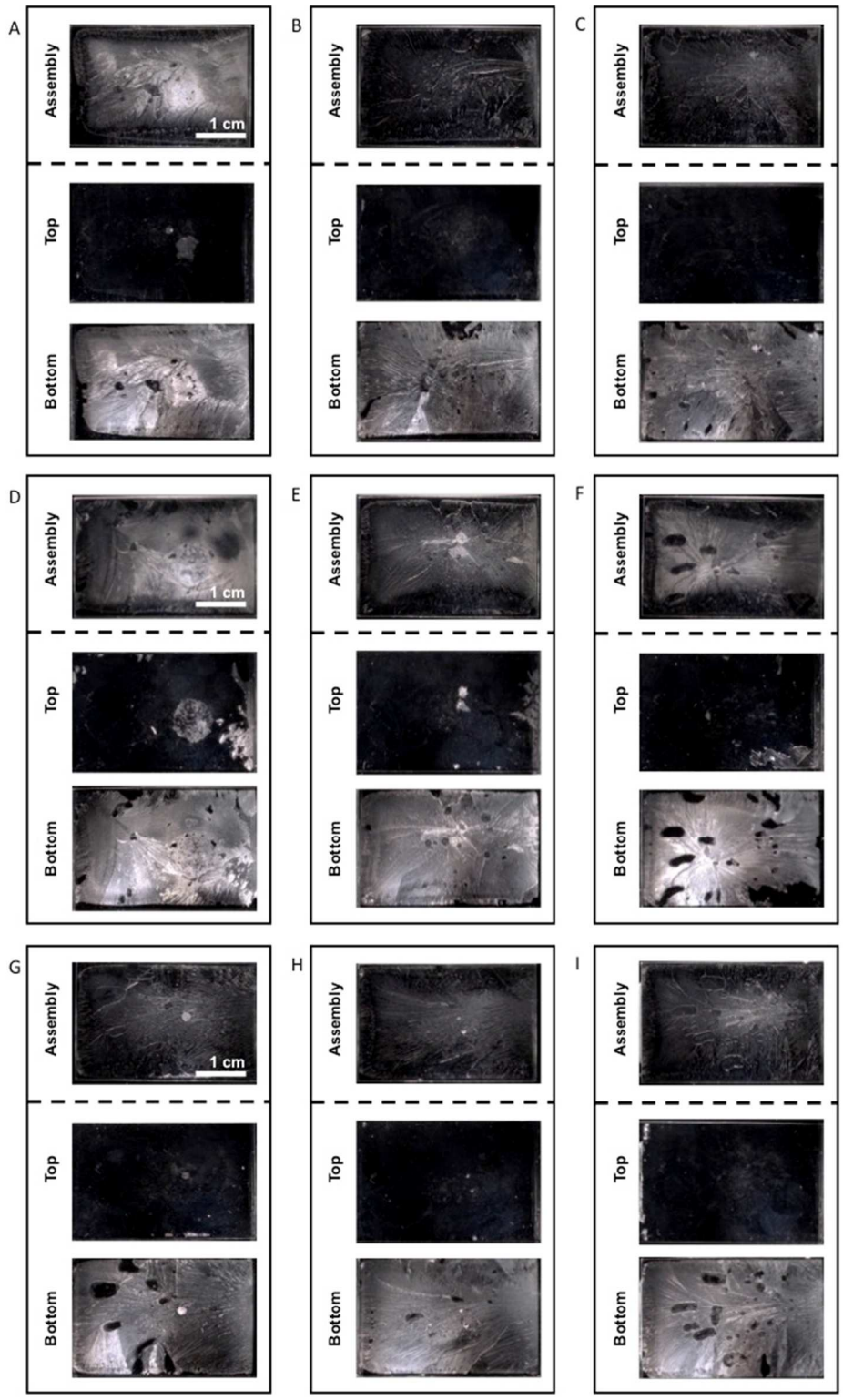

Figure S14. Optical micrographs of $C_{10}F_8$ R1OH/R1F samples before (Assembly) and after (Top, Bottom) lap shearing. A-C, G-I) Samples exhibit primarily adhesive failure. D-F) Samples exhibit primarily adhesive failure with cohesive failure along grain boundaries.

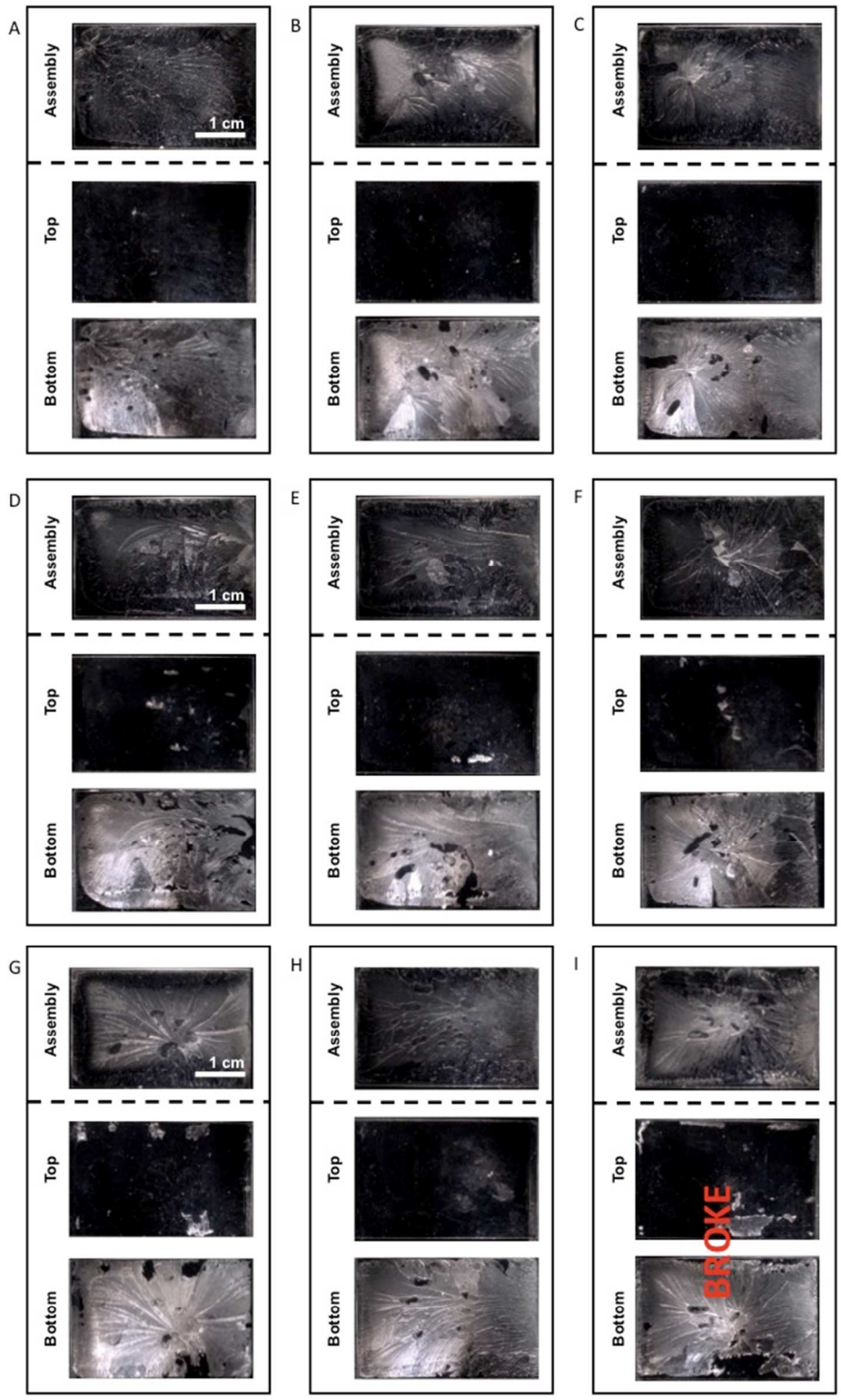

Figure S15. Optical micrographs of $C_{10}F_8$ R1F/R1F samples before (Assembly) and after (Top, Bottom) lap shearing. A-C) Samples exhibit primarily adhesive failure. D-H) Samples exhibit primarily adhesive failure with cohesive failure along grain boundaries. I) Sample sheared prior to mechanical testing.

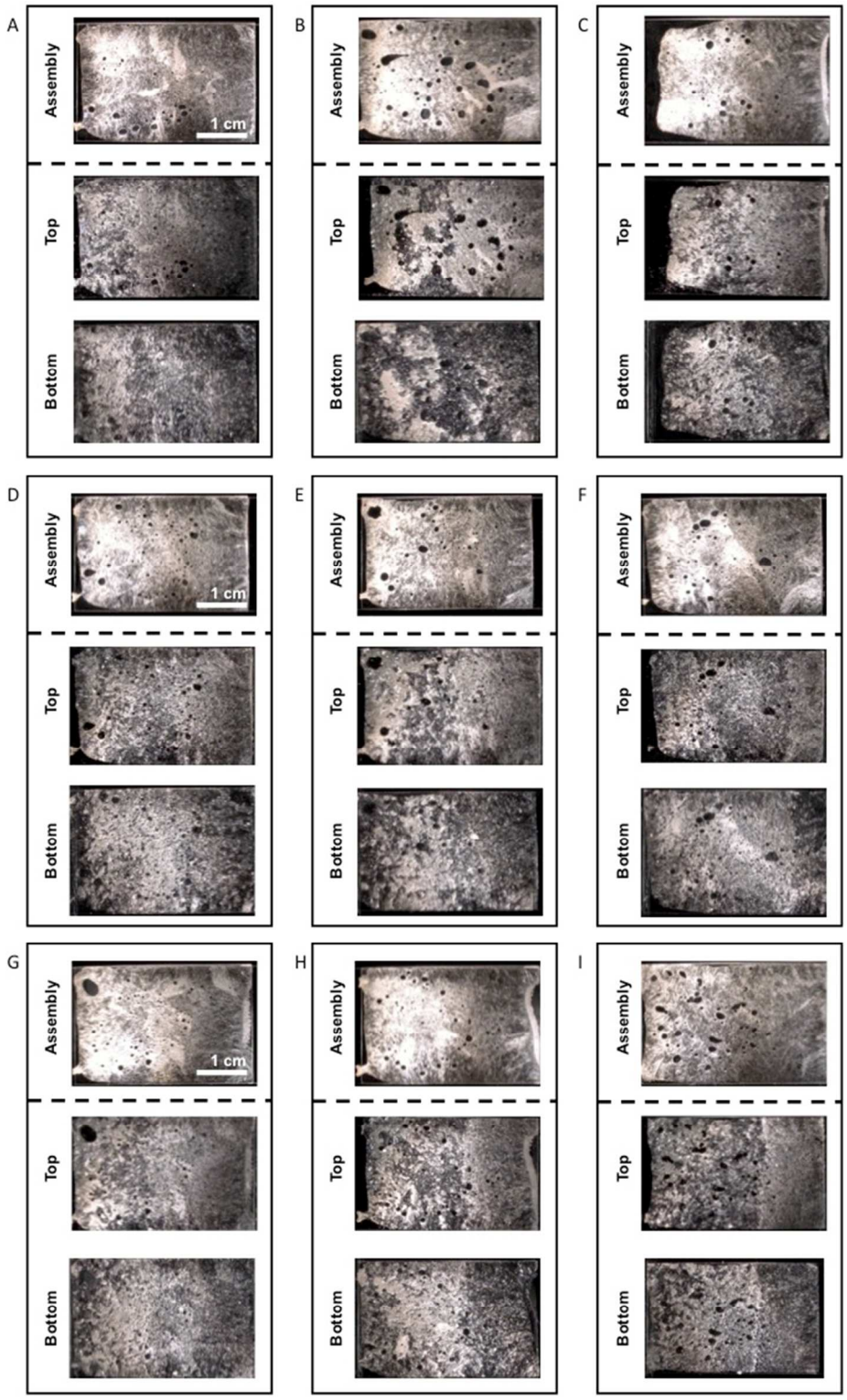

Figure S16. Optical micrographs of $C_{10}H_6(OH)_2$ R1OH/R1OH samples before (Assembly) and after (Top, Bottom) lap shearing. A-I) Samples exhibit primarily cohesive failure.

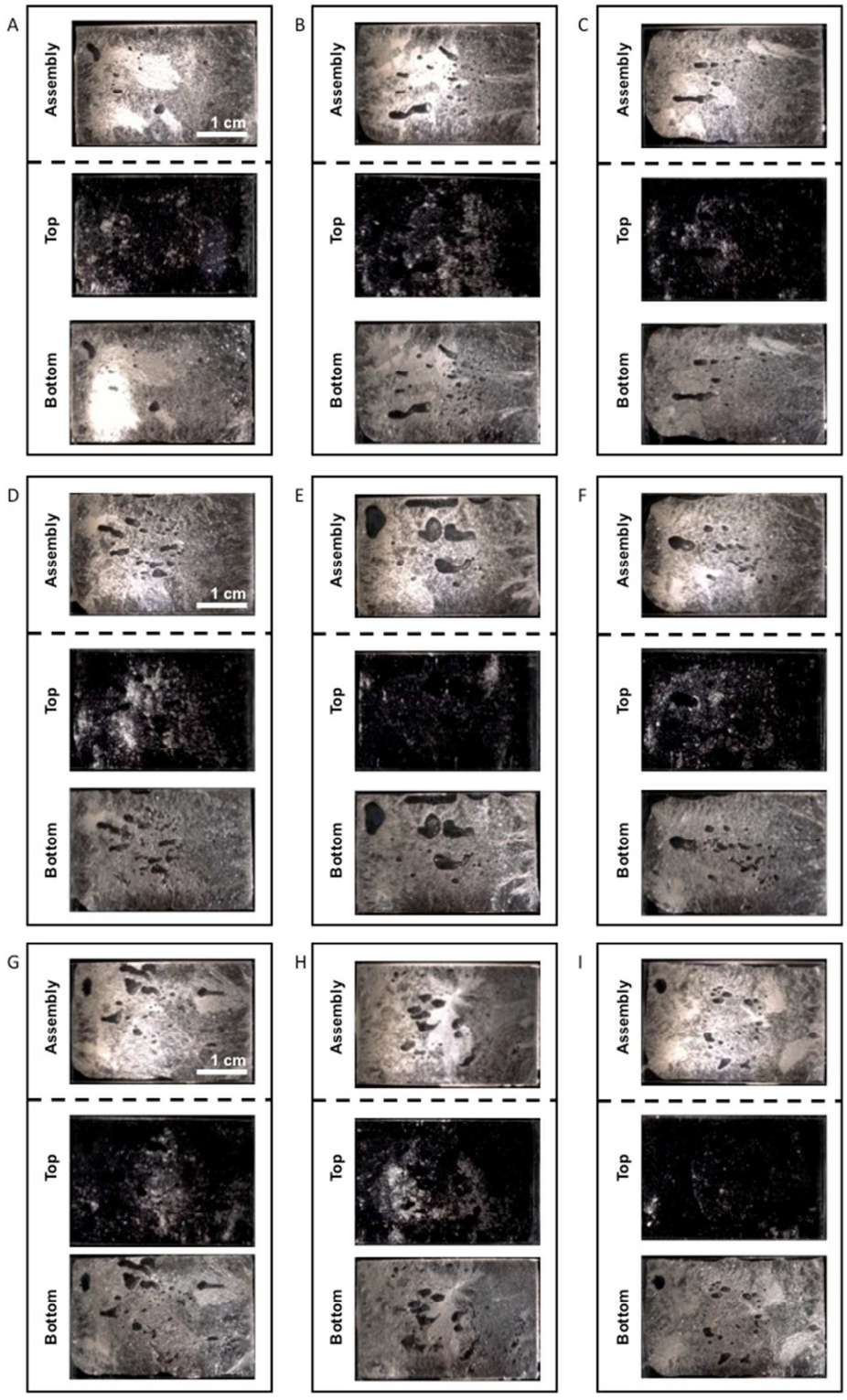

Figure S17. Optical micrographs of $C_{10}H_6(OH)_2$ R1OH/R1F samples before (Assembly) and after (Top, Bottom) lap shearing. A-I) Samples exhibit primarily adhesive failure with cohesive failure.

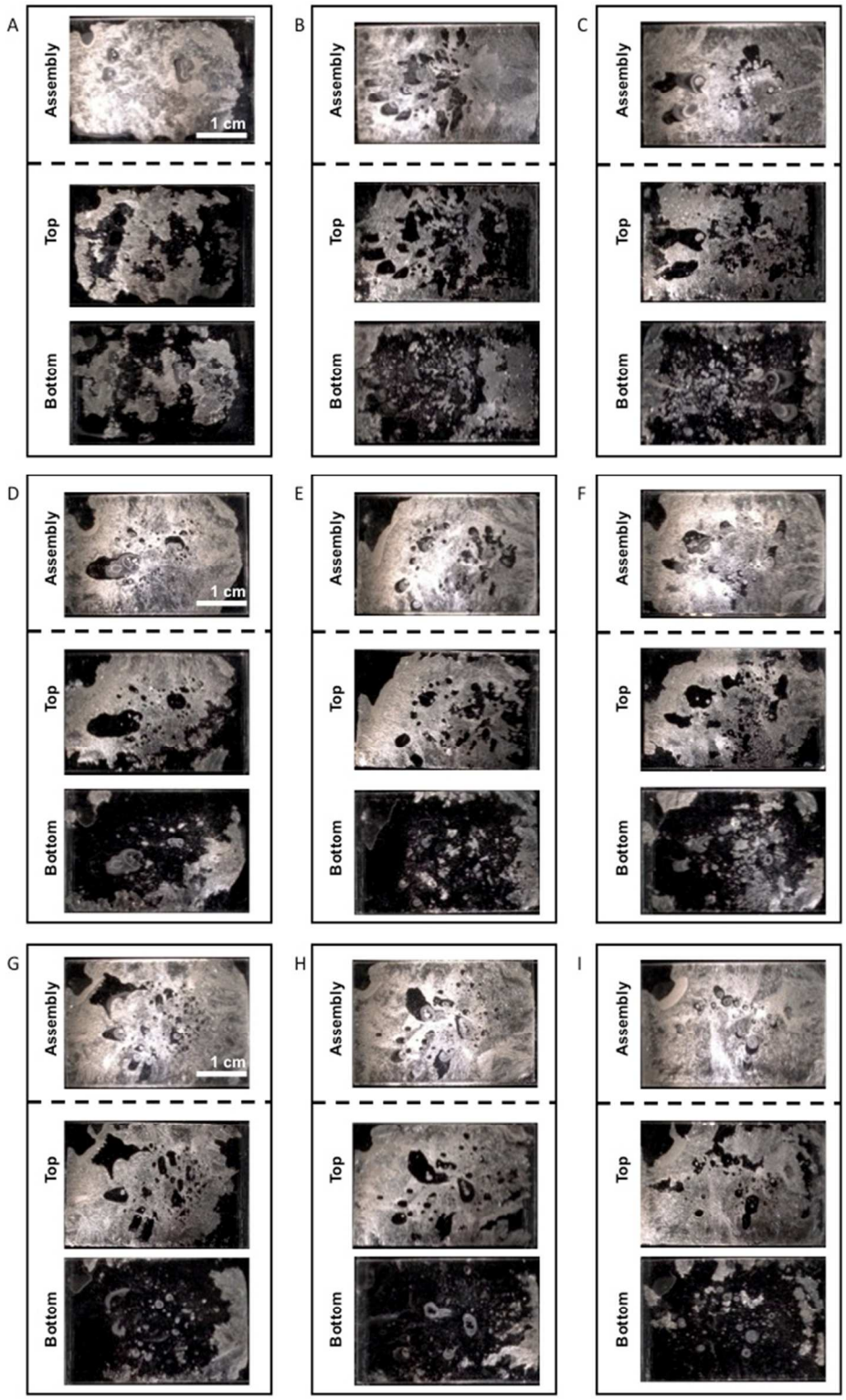

Figure S18. Optical micrographs of $C_{10}H_6(OH)_2$ R1F/R1F samples before (Assembly) and after (Top, Bottom) lap shearing. A-B) Samples exhibit primarily adhesive failure with slight cohesive failure. C) Sample exhibits primarily adhesive failure. D-I) Samples exhibit primarily adhesive failure with cohesive failure along the grain boundaries.

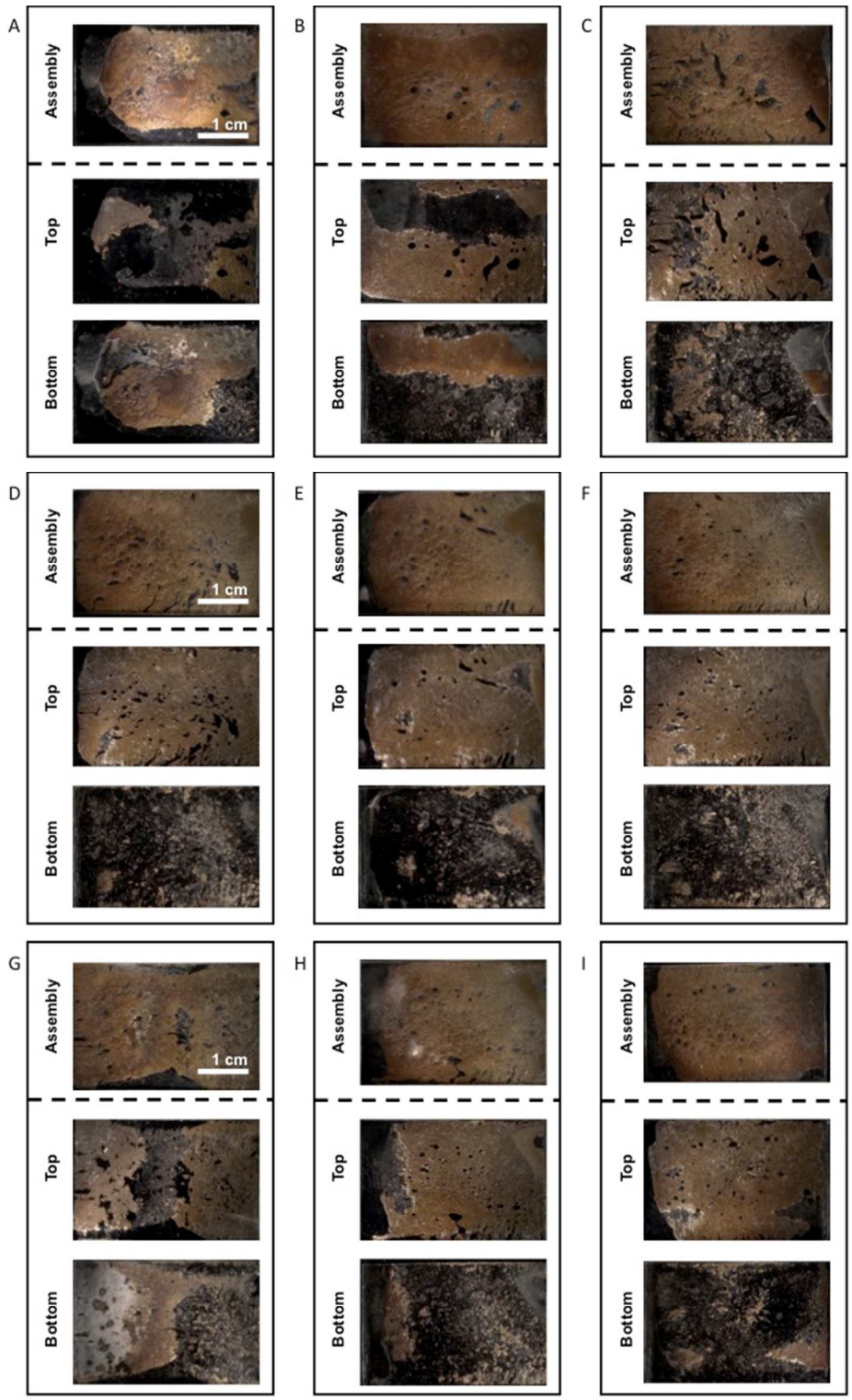

Figure S19. Optical micrographs of $C_{10}H_6(NH_2)_2$ R1OH/R1OH samples before (Assembly) and after (Top, Bottom) lap shearing. A-C) Samples exhibit primarily adhesive failure with cohesive failure along the grain boundaries. D-I) Samples exhibit both adhesive failure and cohesive failure.

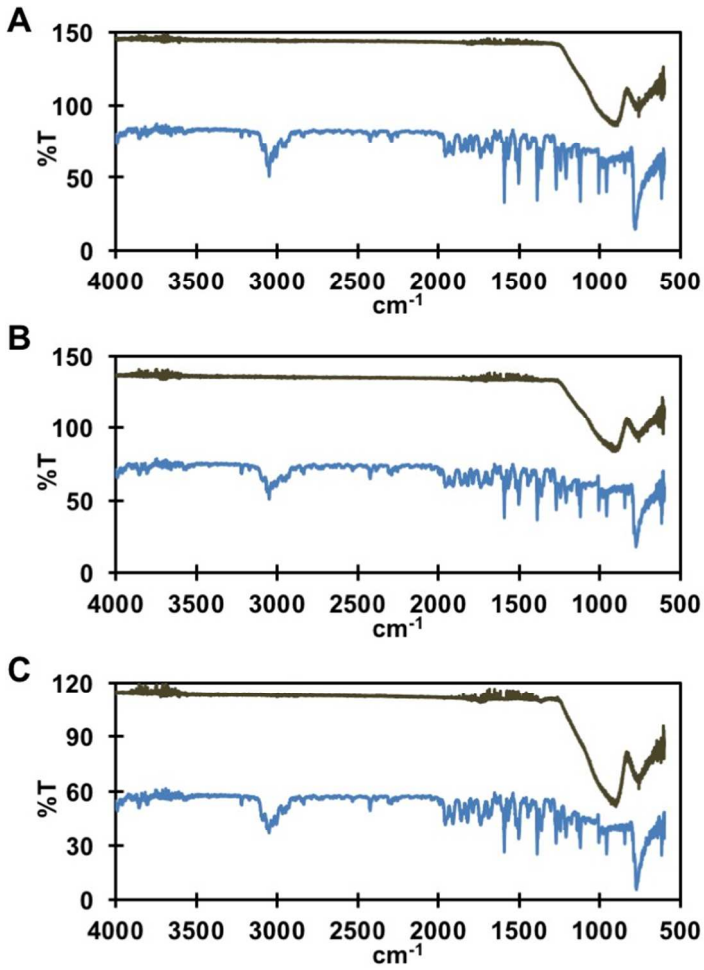

Figure S20. Representative IR spectra for both the top (dark green) and bottom (blue) surfaces from three sheared R1-surface combinations, OH/OH (A), OH/F (B), and F/F (C) melt-bonded with $C_{10}H_8$. A) An IR spectrum recorded on a location with no visible and visible $C_{10}H_8$ on the top (dark green) and bottom (blue) surfaces, respectively, seen in **Figure S10.A**. B) An IR spectrum recorded on a location with no visible and visible $C_{10}H_8$ on the top (dark green) and bottom (blue) surfaces, respectively, seen in **Figure S11.A**. C) An IR spectrum recorded on a location with no visible and visible $C_{10}H_8$ on the top (dark green) and bottom (blue) surfaces, respectively, seen in **Figure S12.A**.

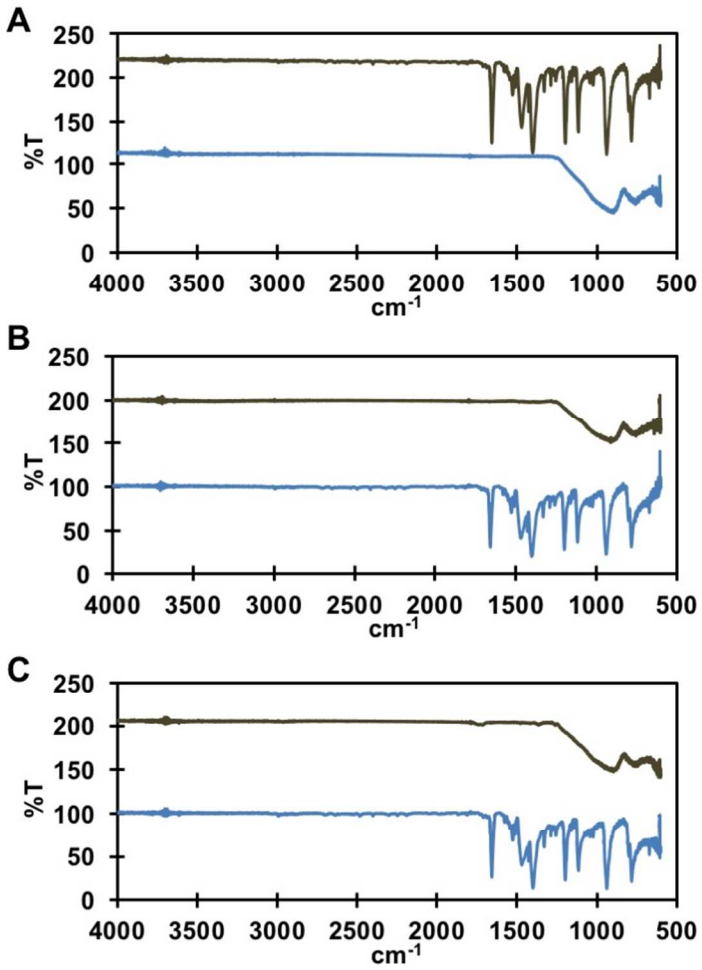

Figure S21. Representative IR spectra for both the top (dark green) and bottom (blue) surfaces from three sheared R1-substrates combinations, OH/OH (A), OH/F (B), and F/F (C) melt-bonded with $C_{10}F_8$. A) An IR spectrum recorded on a location with no visible and visible $C_{10}F_8$ on the top (dark green) and bottom (blue) surfaces, respectively, seen in **Figure S13.A**. B) An IR spectrum recorded on a location with no visible and visible $C_{10}F_8$ on the top (dark green) and bottom (blue) surfaces, respectively, seen in **Figure S14.A**. C) An IR spectrum recorded on a location with no visible and visible $C_{10}F_8$ on the top (dark green) and bottom (blue) surfaces, respectively, seen in **Figure S15.A**.

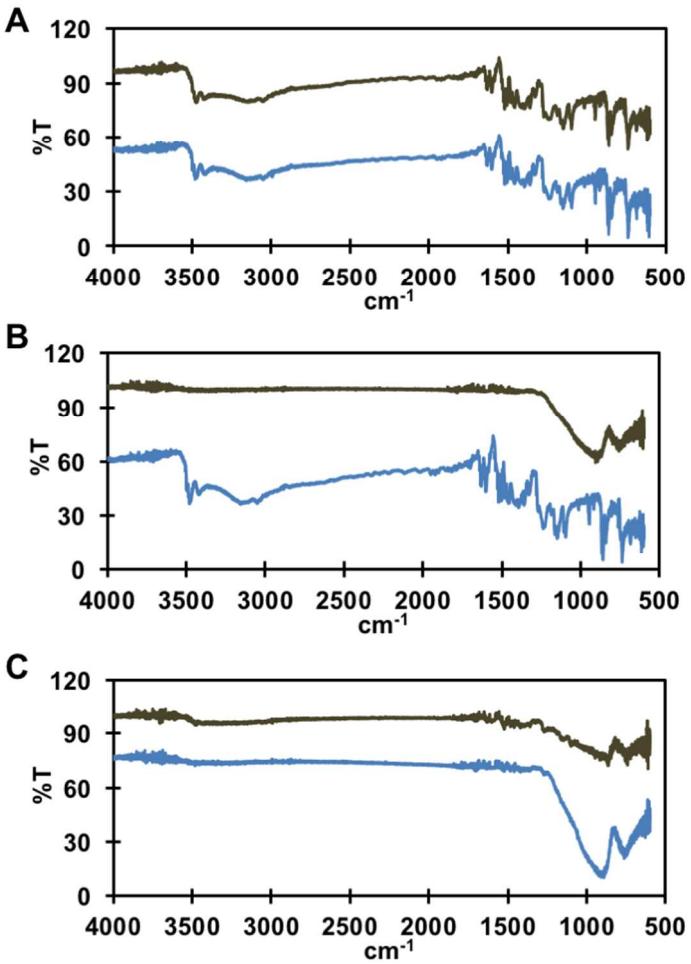

Figure S22. Representative IR spectra for both the top (dark green) and bottom (blue) surfaces from three sheared R1-substrates combinations, OH/OH (A), OH/F (B), and F/F (C) melt-bonded with $C_{10}H_6(OH)_2$. A) An IR spectrum recorded on a location with no visible and visible $C_{10}H_6(OH)_2$ on the top (dark green) and bottom (blue) surfaces, respectively, seen in Figure **S16.A**. B) An IR spectrum recorded on a location with no visible and visible $C_{10}H_6(OH)_2$ on the top (dark green) and bottom (blue) surfaces, respectively, seen in **Figure S17.A**. C) An IR spectrum recorded on a location with no visible and visible $C_{10}H_6(OH)_2$ on the top (dark green) and bottom (blue) surfaces, respectively, seen in **Figure S18.A**.

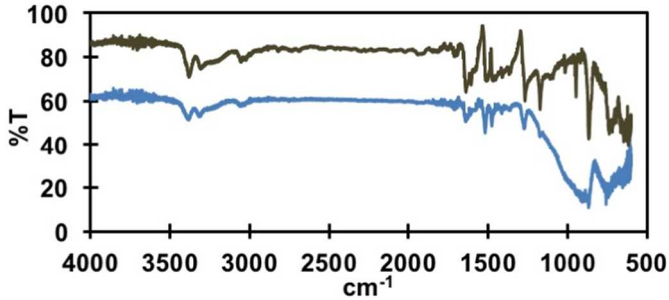

Figure S23. Representative IR spectra for both the top (dark green) and bottom (blue) substrates from R1OH/R1OH melt-bonded with $C_{10}H_6(NH_2)_2$. The IR spectrum was recorded on a location with visible $C_{10}H_6(NH_2)_2$ on both the top (dark green) and bottom (blue) surfaces, respectively, seen in **Figure S19.A**.

Table S10. Summary of measurements taken for assessing the effect of surface chemistry on the mechanism of failure for four PAHs. The mean mass (M_a), film thickness (T_a), surface area (SA_a), load, τ, mass of PAH on bottom slide after shearing (MB_a), and mass of PAH on top slide after shearing (MT_a) based on 8 to 10 measurements. The error in each reported measurement is the standard deviation from the mean based on 7 to 10 measurements.

Adhesive	Substrates (Bot./Top)	M_a (mg)	T_a (μm)	SA_a (cm^2)	Load (N)	τ (N cm^{-2})	MB_a (mg)	MT_a (mg)
$C_{10}H_6(OH)_2$	OH/OH	38 ± 7	30 ± 8	9.0 ± 0.5	270 ± 28	30 ± 3	16 ± 3	21 ± 6
	OH/F	42 ± 6	32 ± 5	9.3 ± 0.3	146 ± 19	16 ± 2	40 ± 6	3 ± 3
	F/F	32 ± 6	30 ± 9	8.7 ± 0.3	116 ± 27	13 ± 3	15 ± 26	15 ± 26
$C_{10}H_6(NH_2)_2$	OH/OH	33 ± 10	34 ± 9	9.2 ± 0.6	153 ± 43	16 ± 4	8 ± 8	25 ± 12
$C_{10}H_8$	OH/OH	42 ± 15	51 ± 23	9.0 ± 0.2	177 ± 31	20 ± 3	22 ± 40	14 ± 33
	OH/F	38 ± 9	39 ± 13	8.5 ± 0.4	94 ± 29	11 ± 3	20 ± 23	12 ± 23
	F/F	41 ± 11	54 ± 15	8.4 ± 0.3	131 ± 27	16 ± 4	35 ± 9	3 ± 3
$C_{10}F_8$	OH/OH	52 ± 13	38 ± 10	9.3 ± 0.2	136 ± 28	15 ± 3	28 ± 40	13 ± 28
	OH/F	52 ± 9	30 ± 9	9.5 ± 0.3	91 ± 35	10 ± 4	68 ±70	1 ± 1
	F/F	54 ± 9	32 ± 6	9.1 ± 0.2	89 ± 35	10 ± 4	44 ± 9	46 ± 137

The mechanism of failure (adhesive or cohesive) may be discerned by visually inspecting optical micrographs (i.e., **Figure S10-19**). $C_{10}H_6(OH)_2$ between two R1OH substrates was the only assembly amongst the assemblies displayed in **Figure S10-19** to demonstrate entirely cohesive failure (fracturing in the bulk of the PAH). The other assemblies showed either almost entirely adhesive failure (**Figure S11.C**) or mixed failure (both cohesive and adhesive, **Figure S19.C**). The MB_a for the F/F and MT_a for OH/F with $C_{10}F_8$ both included glass slides that were chipped during shear testing or transporting between instruments. These chipped glass slides were disregarded in the averages and standard deviations for these samples.

Interestingly, $C_{10}H_6(OH)_2$ and $C_{10}H_6(NH_2)_2$ have similar dipole moments, polarizability, and capacity to H-bond, but have extremely different mechanisms of failure (cohesive and adhesive, respectively) and a difference in τ-values by at least a factor of two. Before moving forward with this discussion it is worth noting the τ-values for $C_{10}H_6(OH)_2$ and $C_{10}H_6(NH_2)_2$ varied between two experiments, from 23 ± 5 (n = 10) and 5 ± 1 (n = 3) in **Figure 2** to 30 ± 3 (n = 10) and 16 ± 4 N cm^{-2} (n = 10) in **Figure S8**, **S9**, and **Table S10**, respectively. Considering τ-values for both $C_{10}H_6(OH)_2$ and $C_{10}H_6(NH_2)_2$ scaled accordingly depending on the experiment, this discrepancy can be taken as an artifact of the experiment, rendering them negligible for this discussion. Continuing the discussion, we have two theories for the differences between $C_{10}H_6(OH)_2$ and $C_{10}H_6(NH_2)_2$; 1) focusing on interfacial interactions and 2) focusing on bulk crystalline properties. The possibility for solid-state acid-base chemistry between the PAH and silanol of the glass

may affect the adhesive behavior at the interface – $C_{10}H_6(OH)_2$, $C_{10}H_6(NH_2)_2$, and the silanol functionality have different pK_a values (9.10, 5.32 and 4-5.5, respectively).[S9] Consequently, one can argue that $C_{10}H_6(NH_2)_2$ will likely deprotonate the silanol, which would lead to efficient charge separation at the interface, leading to facile shearing, similar to mica.[S10] Alternatively, differences in the crystal structure of the two compounds may account for the differences. Both $C_{10}H_6(NH_2)_2$ and $C_{10}H_6(OH)_2$ exhibit planar stacking between organic cores, and orient dipoles oppositely between stacks, but $C_{10}H_6(NH_2)_2$ (crystallized from hydrochloric acid and hydrated) is monoclinic with $P2_1/c$ space group, while $C_{10}H_6(OH)_2$ is orthorhombic with a P_{cab} space group (**SI Section IX**). In terms of performance, $C_{10}H_6(NH_2)_2$ shares molecular, crystalline characteristics of both $C_{10}H_8$ and $C_{10}H_6(OH)_2$ – it fails adhesively, like $C_{10}H_8$, but demonstrates a sensitivity to surface chemistry, like $C_{10}H_6(OH)_2$. These hybrid properties are supported by the differences in crystal structure, which may also account for the differences in adhesive performance.

To enhance the discussion on mechanism of failure, we calculated the surface area of exposed PAH that resulted from either an adhesive or cohesive interface failing. The top and bottom slides were assessed after lap shear testing for cohesive and adhesive failure (**Figure S10-19**). Cohesive failure was considered to be when the bulk of the adhesive fractured. This fracture could occur in a plane parallel or normal to the plane of the glass. Adhesive failure was considered to be when the bulk of the adhesive separated from the glass at the interface without leaving a visible residue. This fracture could only occur parallel to the plane of the glass. To calculate the surface area of cohesive failure, the surface area generated from the cohesive failure was divided by the total surface area (cohesive and adhesive surface area). To calculate the surface area of adhesive failure, the surface area generated from the adhesive failure was divided by the total surface area (cohesive and adhesive surface area). We used Adobe Photoshop and ImageJ 5.0 to measure the surface area of PAH surfaces that failed at either cohesive or adhesive interfaces. To measure the surface area generated from a cohesive failure perpendicular to the plane of the glass the perimeter of the PAH fracture domains were measured using Adobe Photoshop by: 1) placing the image into a canvas in Adobe Photoshop, 2) setting the scale was set using the Measurement Scale in the Image tab, 3) using the Lasso tool to select the features of interest, and 4) meaning the perimeter of the adhesive (perpendicular to the plane of the glass) was measured using

the Measurement function in the Image tab. Once the perimeter was measured, this value was multiplied by the thickness of the adhesive layer to produce a surface area generated by cohesive failure. ImageJ 5.0 was used as described in **SI Section IV.2** to measure the surface area of the PAH that failed at an adhesive interface or cohesive failure parallel to the plane of the glass, see the bottom substrate of **Figure S11.A** for a reference.

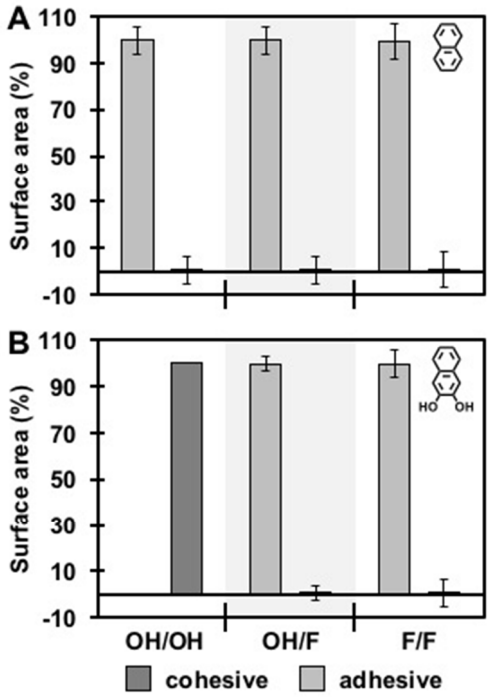

Figure S24. The percent surface area of PAH that failed PAH/PAH interface (cohesive) versus at the PAH/surface interface (adhesive). The light grey bars represent surface area percent that failed at an adhesive interface. The dark grey bars represent surface area percent that failed at a cohesive interface. A) $C_{10}H_8$ melt-bonded between R1-substrates of varying surface chemistry (OH or F) undergoes almost exclusively adhesive failure for all substrate combinations. B) $C_{10}H_6(OH)_2$ melt-bonded between R1OH/R1OH undergoes almost exclusively cohesive failure. The mechanism of failure switches to almost exclusively adhesive failure for R1OH/R1F and R1F/R1F.

IX. Powder X-Ray Diffraction Data and Dominant Exposed Facets

Detailed examination of the Powder X-ray Diffraction (PXRD) patterns for the sheared samples of $C_{10}H_8$ and $C_{10}H_6(OH)_2$ on hydrophilic glass indicated that the melt-bonded materials adopted preferred orientation in comparison to the randomly oriented crystallites in the unmelted, bulk sample (**Figure S26**).[S11-13]

We collected spectra using a Bruker D8 Advance Powder X-ray Diffractometer (PXRD) equipped with a Ge-monochromated 2.2 kW (40 kV, 40 kA) CuKα (λ = 1.54 Å) radiation

source and an NaI scintillation counter detector. The X-ray source and detector for the PXRD defined a plane with the sample holder, and the slide surface was oriented perpendicular to said plane. The range between 2^o and 50^o 2θ was scanned, with a step size of 0.01^o per 2 seconds. Commercially obtained, finely ground PAHs were used as the reference bulk samples, assuming random orientation of crystallites within the sample. Reported single crystal X-ray diffraction data files (.cifs) were used to generate simulated PXRD spectra using Mercury 3.3 (from the Cambridge Crystallographic Data Centre). The unit cell for $C_{10}H_8$, displaying monoclinic symmetry with $P2_1/c$ space group, is defined as a = 7.8242(2), b = 5.9349(1), and c = 8.0997(2) Å.[S14] The unit cell for $C_{10}H_6(OH)_2$, displaying orthorhombic symmetry with P_{cab} space group, is defined as a = 8.555(2), b = 11.296(3), and c = 32.131(8) Å.[S15] Finally, the unit cell for $C_{10}F_8$, displaying monoclinic symmetry with $P2_1/c$ space group, is defined as a = 13.4878(2), b = 4.9209(1), and c = 20.037(3) Å.[S16] It should be noted that the unit cell for $C_{10}H_6(NH_2)_2$ displays monoclinic symmetry with $P2_1/c$ space group when crystallized from hydrochloric acid.[S17] The degree of orientation for major peak changes was quantified using crystallographic preferred orientation (CPO) values for peak ratios between bulk and experimental values. CPOs are calculated using **Equation S3**, where I^X = intensity of peak X, I^Y = intensity of peak Y, ref = bulk sample, and exp = experimental sample.[S18] Peaks X and Y are selected to reflect changes between the bulk sample and the sheared residue. Peak X represents the dominant peak in both samples, and Peak Y one of the top four most dominant peaks in the sheared sample.

$$\mathrm{CPO} = \left(\frac{\mathrm{I^X exp}}{\mathrm{I^Y exp}} - \frac{\mathrm{I^X ref}}{\mathrm{I^Y ref}}\right) / \left(\frac{\mathrm{I^X exp}}{\mathrm{I^Y exp}}\right) \qquad \textbf{(S3)}$$

For $C_{10}H_8$, the CPO values with respect to X = $(21\bar{2})$ and Y = $(11\bar{1})$ are equal to 0.70, 0.84, and 0.54 for OH/OH, OH/F, and F/F, respectively. For $C_{10}H_6(OH)_2$ $(204)/(002)$, CPO values = 0.90, 0.80, 0.74, and 0.54 for OH/OH, OH/F, F/OH and F/F, respectively. Finally, for the same series of substrates, considering peaks $(21\bar{2})$ /$(31\bar{6})$ for $C_{10}F_8$, CPO values = 0.91, 0.90, 0, and 0.96, respectively (see **Figure S25**). When compared to the bulk samples, the percentage of exposed facets change notably upon melt-bonding (**Figure S26-27**). Taken together with the whole PXRD spectra, these CPO values reflect trends in degree of preferred orientation of adhesives with surface chemistry of substrates (**Figure S27**). Collected PXRD spectra, peak assignments, and calculated

Bragg planes for $C_{10}H_8$, $C_{10}H_6(OH)_2$, and $C_{10}F_8$ are shown in **Figures S28, S29,** and **S30**, respectively. Note: PXRD was not performed for $C_{10}H_6(NH_2)_2$, because of the weak adhesion to the glass substrates, making it difficult to prepare a quality sample.

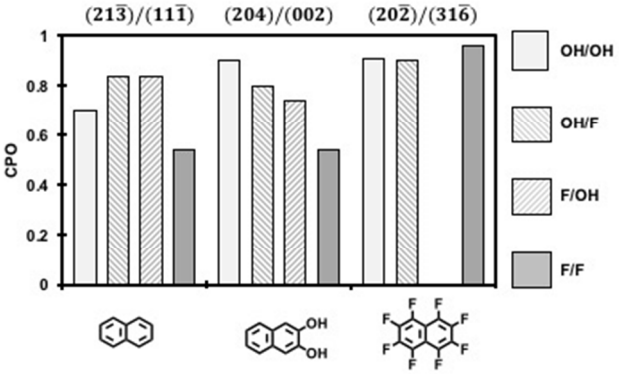

Figure S25. Plot of crystallographic preferred orientation based on PAH structure and substrate. All substrates were R1 glass with a R_a-value of 3 ± 1 nm. CPO values over 0.5 correspond to preferential orientation. Glass backgrounds were subtracted for all experimental intensity values.

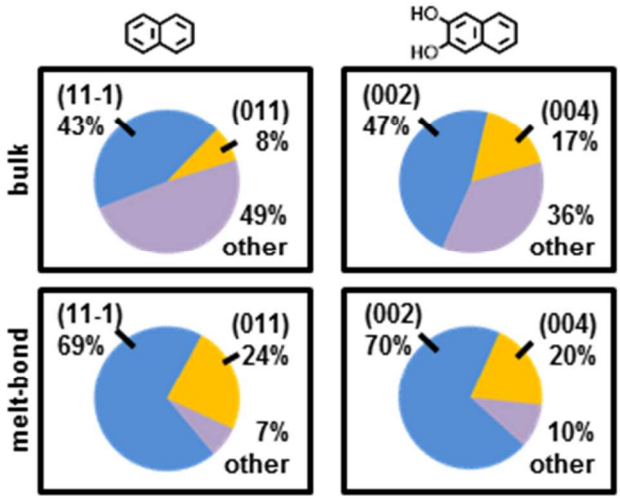

Figure S26. Comparison of the preferential orientation of PAHs on surfaces versus bulk orientation. All samples were prepared and tested on R1-substrates (R_a = 3 ± 1 nm), but the surface chemistry was perturbed. PXRD data for comparison of relative intensity between critical Miller peaks in the bulk sample (top, Si-OH surface functionality) and sheared sample (bottom, average between all surface functionalities).

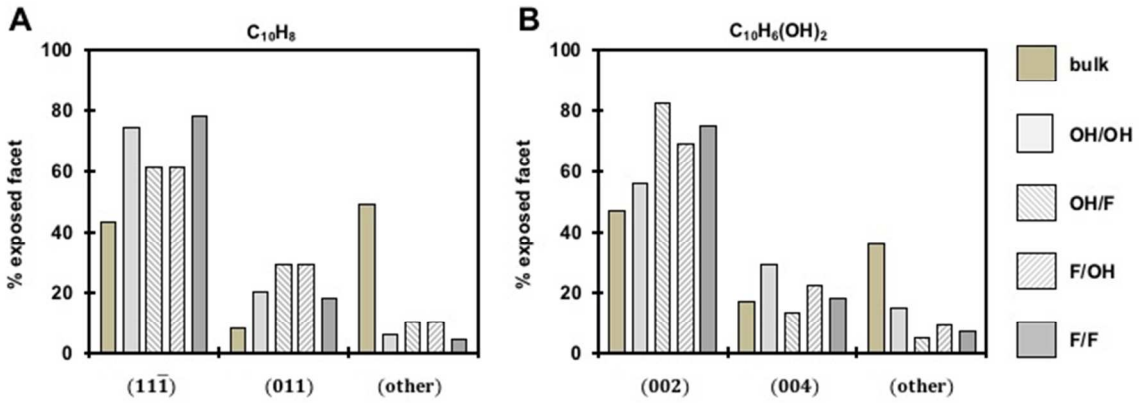

Figure S27. Overall percentage of dominant exposed facets with respect to the substrate surface compared to bulk samples. Both A) ($C_{10}H_8$) and B) ($C_{10}H_6(OH)_2$) were on R1-substrates with varying surface chemistry.

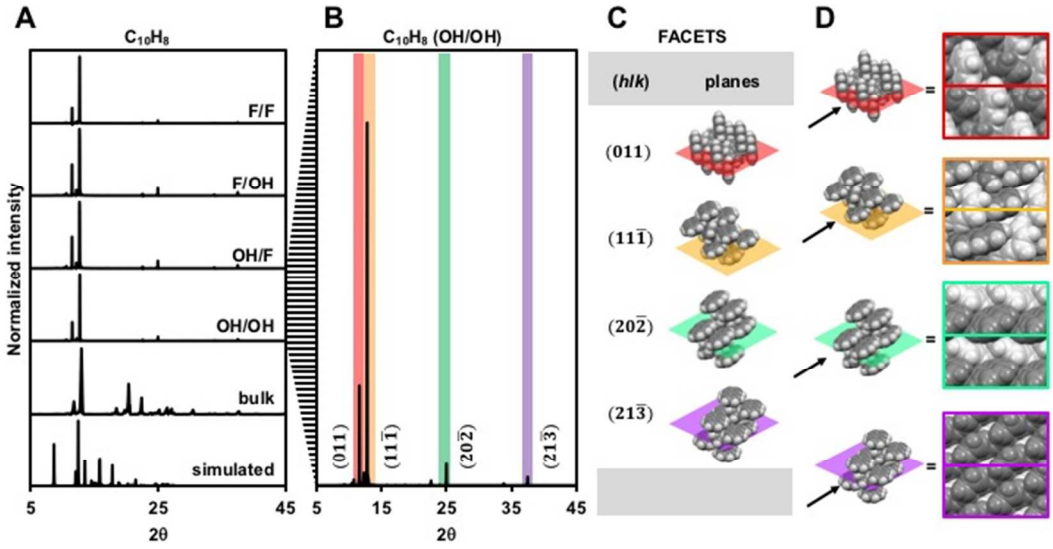

Figure S28. Summary of PXRD data and crystal planes corresponding to dominant peaks for $C_{10}H_8$. A) Representative PXRD traces for exposed $C_{10}H_8$ resting on the bottom substrate (bottom/top) that was melt-bonded between various substrate combinations. B) OH/OH spectra with dominant exposed facets labeled. C) Crystallographic planes corresponding to each dominant peak in the PXRD spectra, reflecting the orientation of the unit cell with respect to the substrate surface. D) Side-on view of the crystal structure for each exposed facet. Arrows corresponds to line of sight, and $C_{10}H_8$ monomers are falsely colored to emphasize crystal packing.

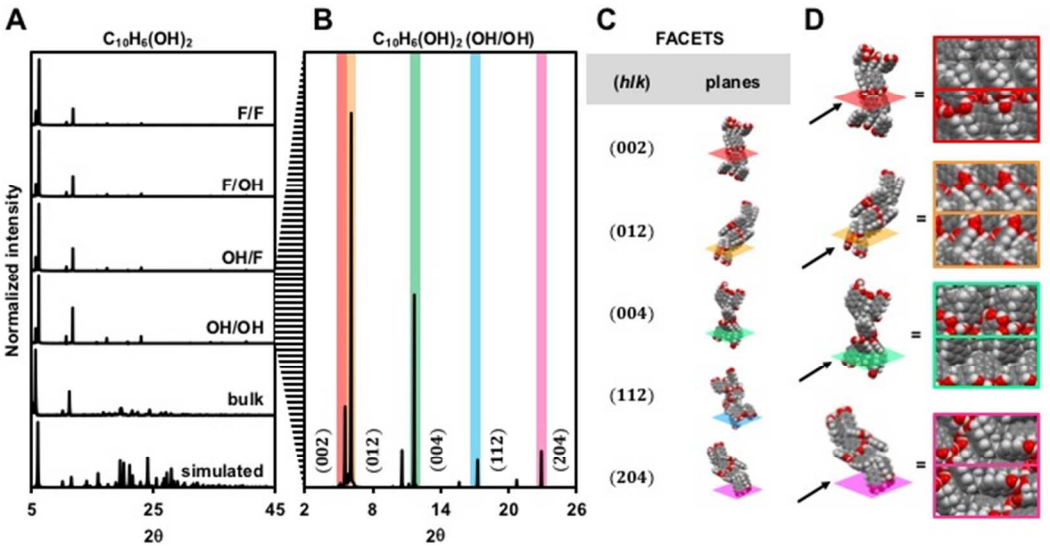

Figure S29. Summary of powder X-ray diffraction data and crystal planes corresponding to dominant peaks for $C_{10}H_6(OH)_2$. A) Representative PXRD traces for exposed $C_{10}H_6(OH)_2$ resting on the bottom substrate (bottom/top) that was melt-bonded between various substrate combinations. B) OH/OH spectra with dominant exposed facets labeled. C) Crystallographic planes corresponding to each dominant peak in the PXRD spectra, reflecting the orientation of the unit cell with respect to the substrate surface. D) Side-on view of the crystal structure for each exposed facet. Arrows corresponds to line of sight.

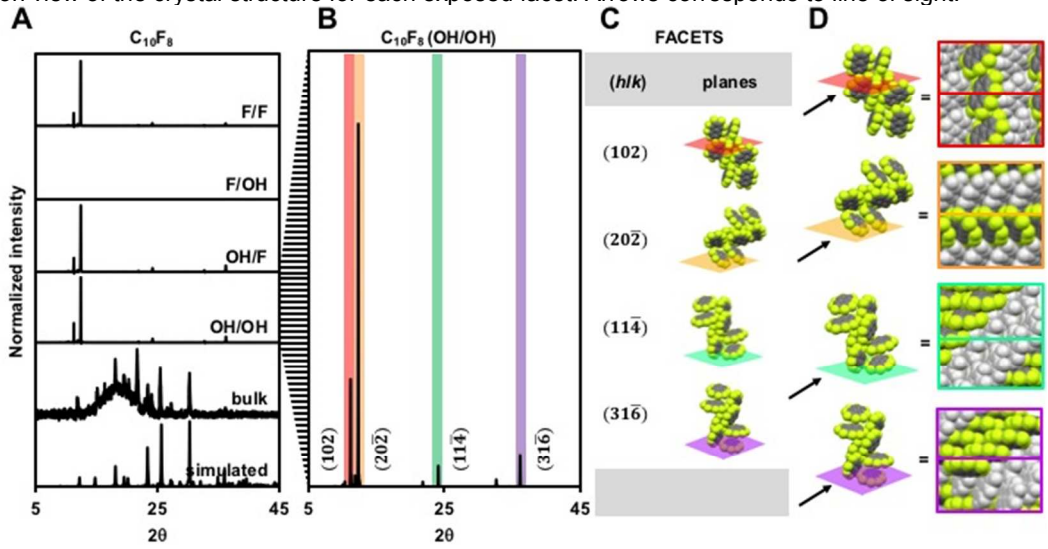

Figure S30. Summary of powder X-ray diffraction data and crystal planes corresponding to dominant peaks for $C_{10}F_8$. A) Representative PXRD traces for exposed $C_{10}H_8$ resting on the bottom substrate (bottom/top) that was melt-bonded between various substrate combinations. B) OH/OH spectra with dominant exposed facets labeled. C) Crystallographic planes corresponding to each dominant peak in the PXRD spectra, reflecting the orientation of the unit cell with respect to the substrate surface. D) Side-on view of the crystal structure for each exposed facet. Arrows corresponds to line of sight, and $C_{10}F_8$ monomers are falsely colored to emphasize crystal packing.

X. Scanning Electron Microscopy of Crystal Morphologies

Figure S31-32 are a series of images of $C_{10}H_8$ and $C_{10}H_6(OH)_2$ on R1OH obtained by a Scanning Electron Microscope (SEM, Hitachi TM3000). These samples were prepared by the procedure described in **SI Section III.1**. The samples were then sheared apart

manually and 1 × 2 cm portions of interest (areas with PAH present) were cut from one of the sheared substrates. The 1 × 2 cm segment was adhered to the cryostage using double-coated carbon conductive tape (Ted Pella, 16084-7). The SEM was set to a “low vacuum mode” with a pressure of 0.8 Torr, accelerating voltage of 15.0 kV, and cryostage set to -130 °C with a gaseous secondary electron (GSE) detector. The instrument was operated in “low vacuum mode” with a cryostage to slow or prevent sublimation of PAHs under analysis.

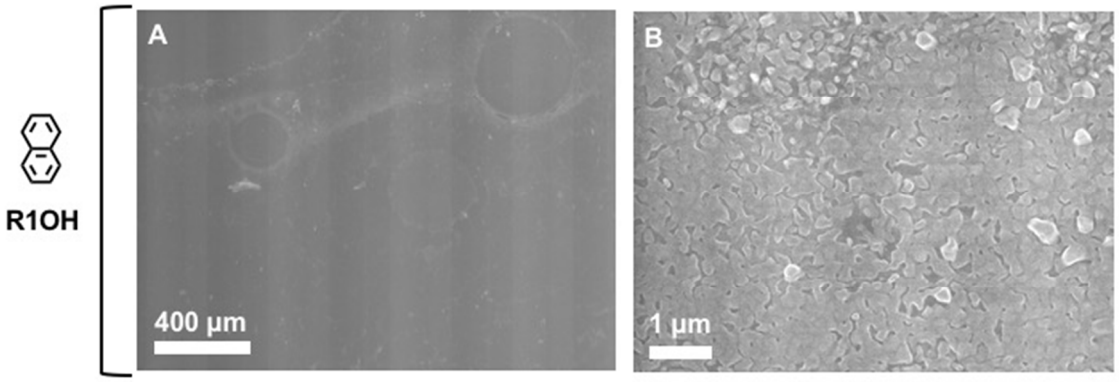

Figure S31. Images of crystalline features for $C_{10}H_8$ melt-bonded between two R1OH substrates taken with SEM. A-F) Images show the size and morphology of $C_{10}H_8$ when melt-bonded between two R1OH substrates.

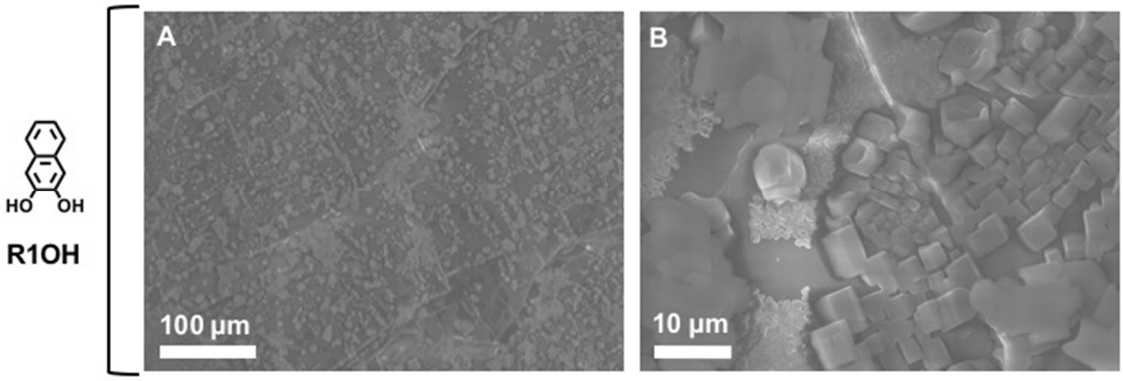

Figure S32. Images of crystalline features for $C_{10}H_6(OH)_2$ melt-bonded between two R1OH substrates taken with SEM. A-F) Images show the size and morphology of $C_{10}H_6(OH)_2$ when melt-bonded between two R1OH substrates.

XI. Polarized Light Microscopy

Images using a Nikon E200 POL were obtained of $C_{10}H_8$, $C_{10}F_8$, and $C_{10}H_8(OH)_2$ between R1OH/R1OH, R1OH/R1F, and R1F/R1F. Images were only captured for $C_{10}H_8(NH_2)_2$ between R1OH/R1OH because it was ineffective at bonding silanized surfaces. Images were taken with the stage at 0°, 45°, and 90° with the objective and

ocular lens set to four and ten times magnification, respectively, for a total of forty times magnification. A standard scale bar was imaged to assist in determining the scale of features in samples. All the images for the samples are displayed in **Figure S33-42**.

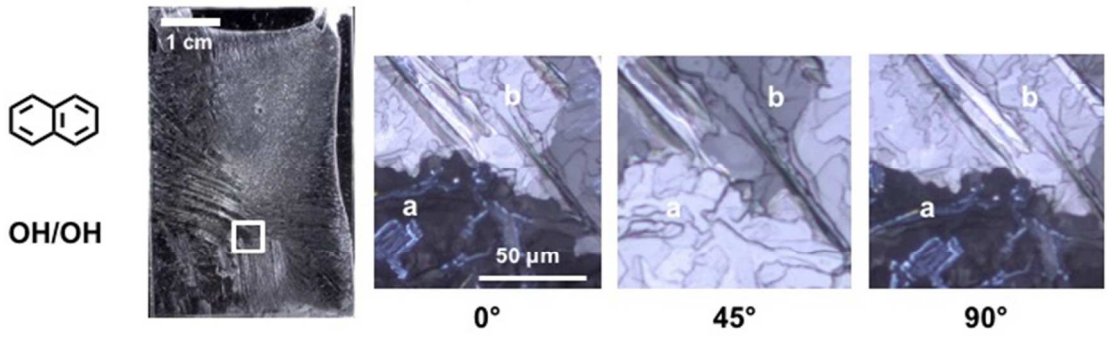

Figure S33. Cross polarized light images of R1OH/R1OH melt-bonded by $C_{10}H_8$, displaying polycrystallinity. The stage the sample rested on was rotated from 0° to 45° to 90° to show the changing extinction (dark versus bright areas) of different domains. Different crystalline domains are labeled with an *a* and *b*.

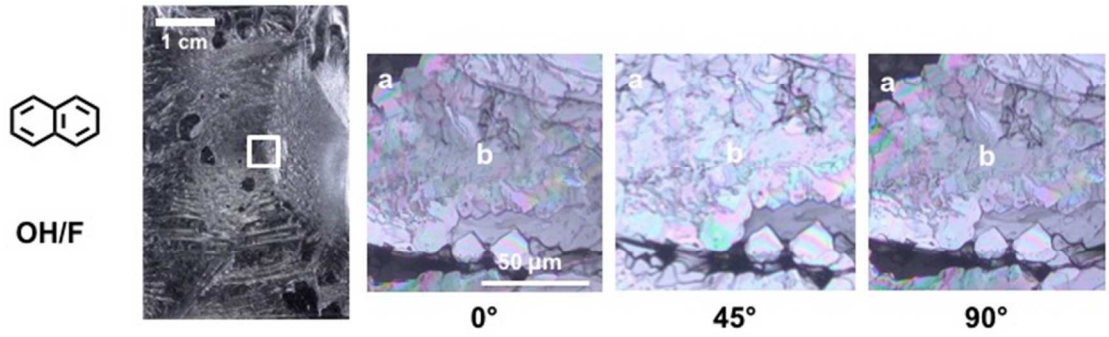

Figure S34. Cross polarized light images of R1OH/R1F melt-bonded by $C_{10}H_8$, displaying polycrystallinity. The stage the sample rested on was rotated from 0° to 45° to 90° to show the changing extinction (dark versus bright areas) of different domains. Different crystalline domains are labeled with an *a* and *b*.

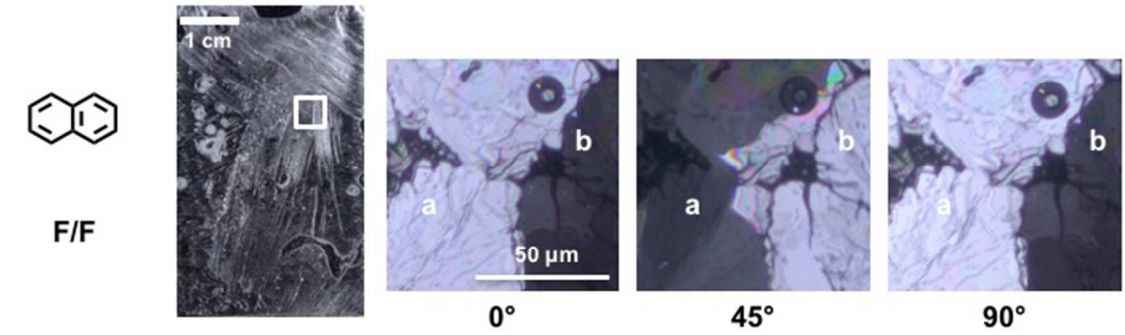

Figure S35. Cross polarized light images of R1F/R1F melt-bonded by $C_{10}H_8$, displaying polycrystallinity. The stage the sample rested on was rotated from 0° to 45° to 90° to show the changing extinction (dark versus bright areas) of different domains. Different crystalline domains are labeled with an *a* and *b*.

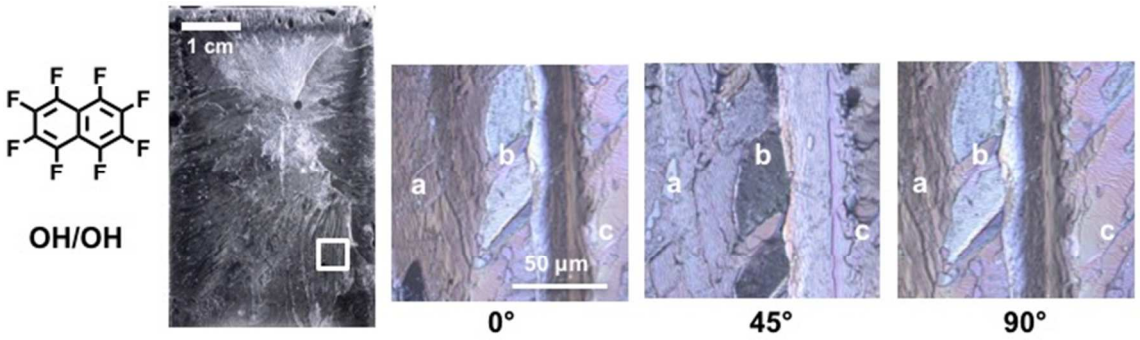

Figure S36. Cross polarized light images of R1OH/R1OH melt-bonded by $C_{10}F_8$, displaying polycrystallinity. The stage the sample rested on was rotated from 0° to 45° to 90° to show the changing extinction (dark versus bright areas) of different domains. Different crystalline domains are labeled with an *a*, *b*, and *c*.

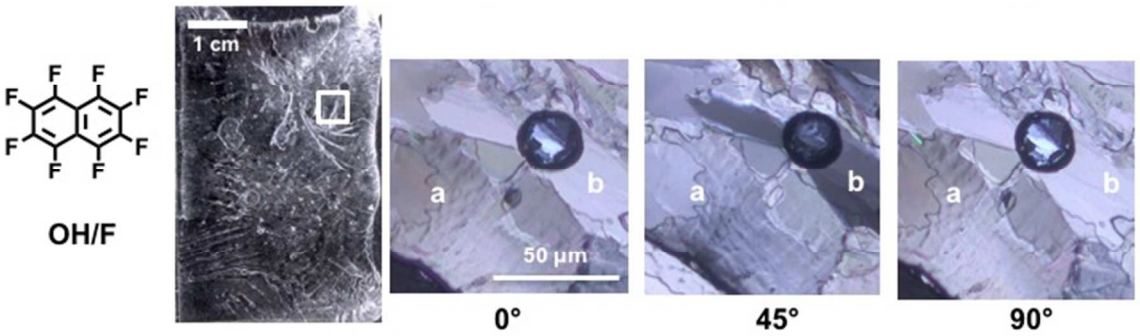

Figure S37. Cross polarized light images of R1OH/R1F melt-bonded by $C_{10}F_8$, displaying polycrystallinity. The stage the sample rested on was rotated from 0° to 45° to 90° to show the changing extinction (dark versus bright areas) of different domains. Different crystalline domains are labeled with an *a* and *b*.

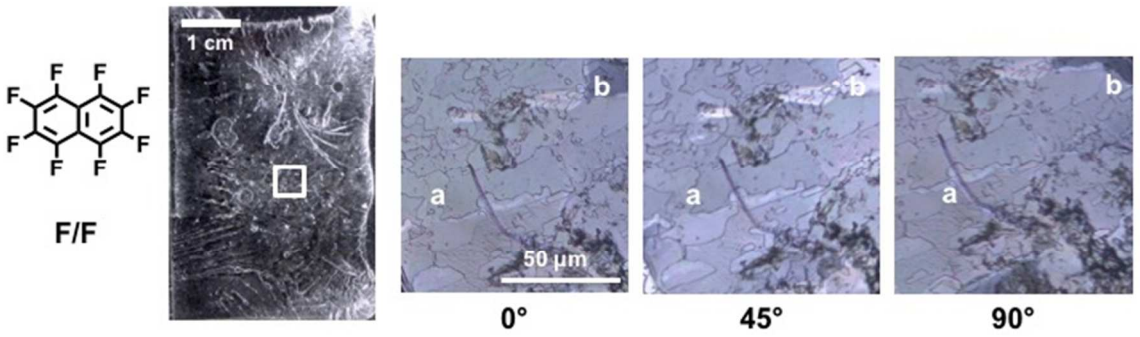

Figure S38. Cross polarized light images of R1F/R1F melt-bonded by $C_{10}F_8$, displaying polycrystallinity. The stage the sample rested on was rotated from 0° to 45° to 90° to show the changing extinction (dark versus bright areas) of different domains. Different crystalline domains are labeled with an *a* and *b*.

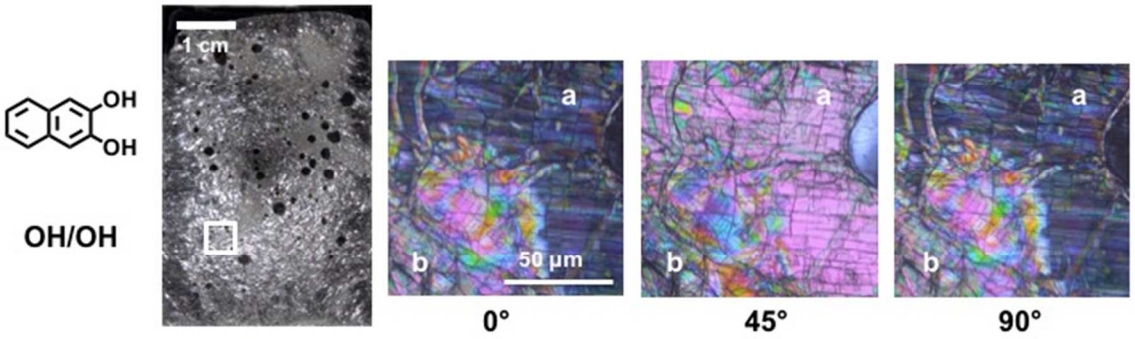

Figure S39. Cross polarized light images of R1OH/R1OH melt-bonded by $C_{10}H_8(OH)_2$, displaying polycrystallinity. The stage the sample rested on was rotated from 0° to 45° to 90° to show the changing extinction (dark versus bright areas) of different domains. Different crystalline domains are labeled with an *a* and *b*.

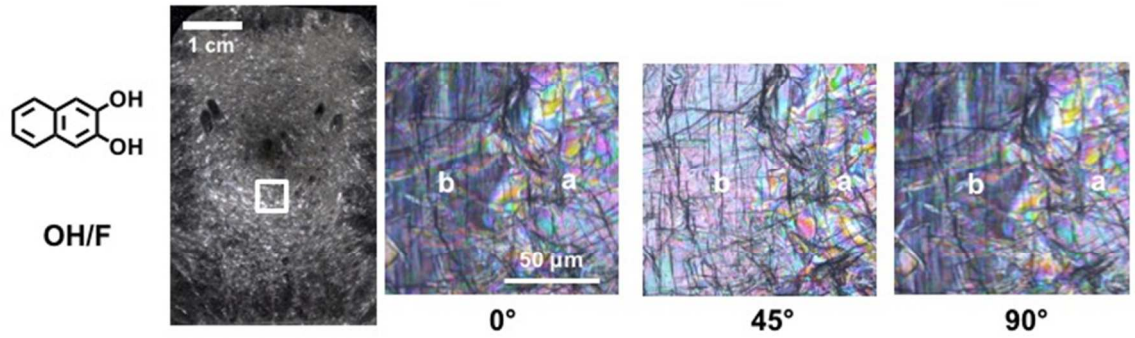

Figure S40. Cross polarized light images of R1OH/R1F melt-bonded by $C_{10}H_8(OH)_2$, displaying polycrystallinity. The stage the sample rested on was rotated from 0° to 45° to 90° to show the changing extinction (dark versus bright areas) of different domains. Different crystalline domains are labeled with an *a* and *b*.

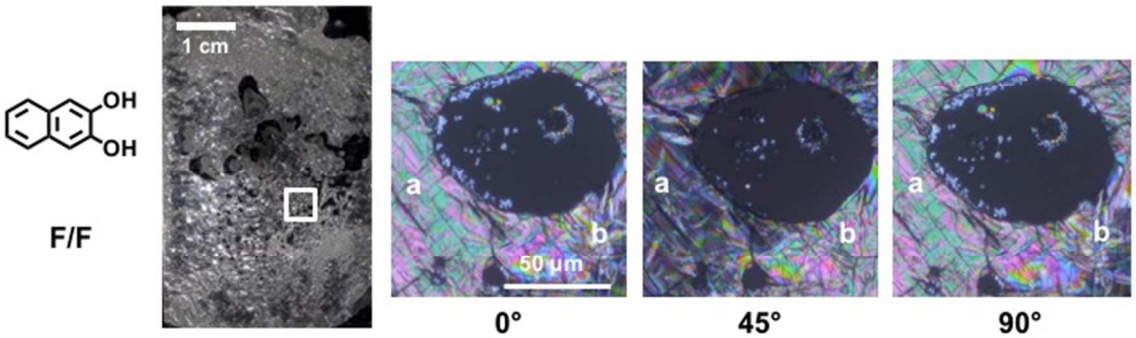

Figure S41. Cross polarized light images of R1F/R1F melt-bonded by $C_{10}H_8(OH)_2$, displaying polycrystallinity. The stage the sample rested on was rotated from 0° to 45° to 90° to show the changing extinction (dark versus bright areas) of different domains. Different crystalline domains are labeled with an *a* and *b*.

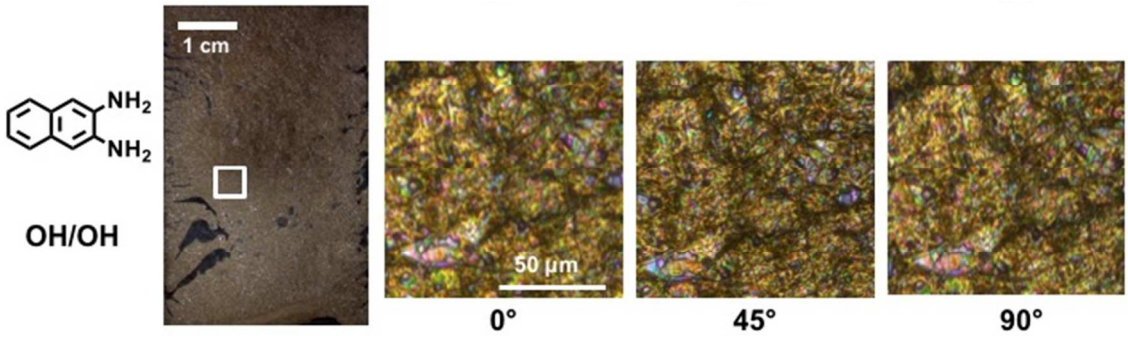

Figure S42. Cross polarized light images of R1OH/R1OH melt-bonded by $C_{10}H_8(NH_2)_2$, displaying polycrystallinity. The stage the sample rested on was rotated from 0° to 45° to 90° to show the changing extinction (dark versus bright areas) of different domains. Different crystalline domains are labeled with an *a* and *b*.

XII. Melt-bonding and Release of Substrates by Sublimation

Phase transitions during melt-bonding and sublimation can be described by the Clapeyron (**Equation S3**) and Clausius-Clapeyron equation (**Equation S4**) equations.[S19] In these equations, P_1 and P_2 (both in kPa units) and T_1 and T_2 (both in K units) are the pressure and temperature at two points along a phase-transition curve of a chemical substance. For the process of melt-bonding, ΔH_{fus} (kJ mol^{-1}) is the molar enthalpy of fusion and ΔV_m (m^3 mol^{-1}) is the change in molar volume upon phase transition (assumed to be constant for the phase transition from solid to liquid). For the process of release, ΔH_{sub} (kJ mol^{-1}) is the molar enthalpy of sublimation. The gas constant is represented by R (8.314 $\times$ 10^{-3} kJ K^{-1} mol^{-1}). The Joback method[S20] was used to estimate the ΔH_{fus} of $C_{10}H_6(NH_2)_2$, $C_{10}H_6(OH)_2$, and $C_{16}H_{10}O$, and the ΔH_{sub} of $C_{10}H_6(NH_2)_2$. This method involves summing the group contribution from each constituent of the compound (i.e. –CH_2– or –OH). The ΔH_{fus} and ΔH_{sub} values and references are summarized in **Table S11**. No error was calculated for the ΔH_{fus} and ΔH_{sub} values estimated by the Joback method.[S20]

$$\boldsymbol{P_2 = P_1 + \left(\frac{\Delta H_{fus}}{\Delta V_m}\right) ln \left(\frac{T_2}{T_1}\right)} \quad \textbf{(S3)}$$

$$\boldsymbol{ln\left(\frac{P_1}{P_2}\right) = \left(\frac{\Delta H_{sub}}{R}\right)\left(\frac{1}{T_2} - \frac{1}{T_1}\right)} \quad \textbf{(S4)}$$

Table S11. Summary of citations for enthalpies of fusion (ΔH_{fus}, kJ mol^{-1}) and sublimation (ΔH_{sub}, kJ mol^{-1}). The ΔH_{fus} and ΔH_{sub} in this table were used in **Figure 1b** and **1c** in the main text, respectively. The ΔH_{sub} for $C_{10}H_8$, $C_{10}H_7OH$, $C_{10}F_8$, and $C_{14}H_{10}$ were used to make qualitative estimates of the time to release for experiments summarized in **Table S12** and **Section XIII**.

Compound	ΔH_{fus} (kJ mol^{-1})	Ref. for ΔH_{fus}	ΔH_{sub} (kJ mol^{-1})	Ref. for ΔH_{sub}
$C_{10}H_8$	19.6 ± 0.4	S22, S27	71 ± 0.4	S26,S28
$C_{10}H_7(OH)$	20.9 ± 0.2	S21, S27	88 ± 3	S28
$C_{10}H_6(NH_2)_2$	24.3	S20	87	S20
$C_{10}H_6(OH)_2$	22.3	S20	110 ± 1	S28
$C_{10}F_8$	17.6 ± 0.5	S23	79 ± 3	S28
$C_{14}H_{10}$	29.8 ± 0.5	S21, S27	99 ± 3	S24, S28
$C_{14}H_9(OOH)$	34.7 ± 0.3	S25	120 ± 4	S25
$C_{16}H_{10}$	16.7 ± 0.5	S21, S27	98 ± 3	S28
$C_{16}H_{10}O$	29.0	S20	110 ± 4	S29

The Clapeyron equation assumes the ΔH_{sub} is constant throughout the phase transition. The Clausius-Clapeyron equation builds on this assumption with two additional assumptions: (i) the molar volume of a solid is negligibly small in comparison to the molar volume of a gas, and (ii) the volume of the gaseous phase can be approximated by the ideal gas equation.

Release by sublimation was demonstrated using R1OH and an aluminum grate. The aluminum grate was 5.9 × 4.2 cm and 1.64 mm thick with pores 0.4 cm in diameter spaced 0.89 mm apart in staggered rows. Four R1OH–substrates (2.5 × 2.1 cm, 2.5 × 1.9 cm, 2.5 × 1.6 cm, and 2.5 × 1.6 cm) were melt-bonded using $C_{10}F_8$ (53 mg), $C_{10}H_8$ (49 mg), $C_{10}H_7OH$ (65 mg), and $C_{16}H_{10}$ (38 mg), respectively. R1OH substrates were melt-bonded to the aluminum grate by sandwiching the adhesive between the R1OH substrate and aluminum grate and heating on a hotplate. The samples were then released by sublimation under the conditions summarized in **Table S12**. Additionally, **Table S12** includes the temperature of the hotplate (T_{hp}) the sublimer rested on, time to release (T_r), and the observed rate of sublimation (R_s). The T_r was the time taken for the substrate to fall away from the grate.

Table S12. Summary of the parameters for subliming various PAHs from between R1OH and an aluminum grate. The change in the standard enthalpy of sublimation (ΔH_{sub}) was used as a metric to select the four PAHs that would give a range of rate of sublimation (R_s). The melting point (M_p) was used as a limit for setting the temperature of the hot plate (T_{hp}). The mass of adhesive (Mass) and time to release (T_r) were recorded.

Adhesive	M_p (°C)	ΔH_{sub} (kJ mol^{-1})	Mass (mg)	T_{hp} (°C)	Vp_{Thp} (kPa)	T_r (min)	R_s (mg min^{-1})
$C_{10}F_8$	87	79	58	75	560	7	10
$C_{10}H_8$	80	71	49	70	0.5	45	1.1
$C_{10}H_7OH$	121	88	65	120	0.2	90	0.4

$C_{16}H_{10}$	147	100	38	140	8×10^{-3}	420	0.1

XIII. Sequential Melt-bonding and Release of Substrates by Sublimation

Two separate glass substrates, "Dartmouth" (2.5 × 1.6 cm), and "College" (2.5 × 1.6 cm), cut from R1OH substrates using a glass cutter, were sequentially bonded and released from the same carrier surface using two adhesives, $C_{10}H_8$ (25 mg) and $C_{10}H_7OH$ (28 mg) (**Figure S43**). PAHs ($C_{10}H_8$ and $C_{10}H_7OH$) were chosen for their difference in melting temperatures and standard enthalpies of sublimation, 80.5 °C and 71 ± 0.4 kJ mol^{-1},[S27,S26] and, 121 °C and 88 ± 3 kJ mol^{-2},[S27,S28] respectively. The large aluminum grate was used as the permeable carrier. The differences in melting temperature allowed for sequential bonding. "Dartmouth" was bonded first using $C_{10}H_7OH$ followed by "College" using $C_{10}H_8$. The differences in the standard enthalpy of sublimation allowed for sequential removal of the PAH and subsequent release of the substrate. The removal of $C_{10}H_8$ was facilitated first at 7 kPa and 70 °C, releasing "College". The pressure was maintained, while temperature was increased to 115 °C to facilitate the removal $C_{10}H_7OH$, releasing "Dartmouth". The mass was taken for all substrates before bonding, once bonded as a system, and after all surfaces had separated. There was no measurable mass of PAH residue on any of the surfaces.

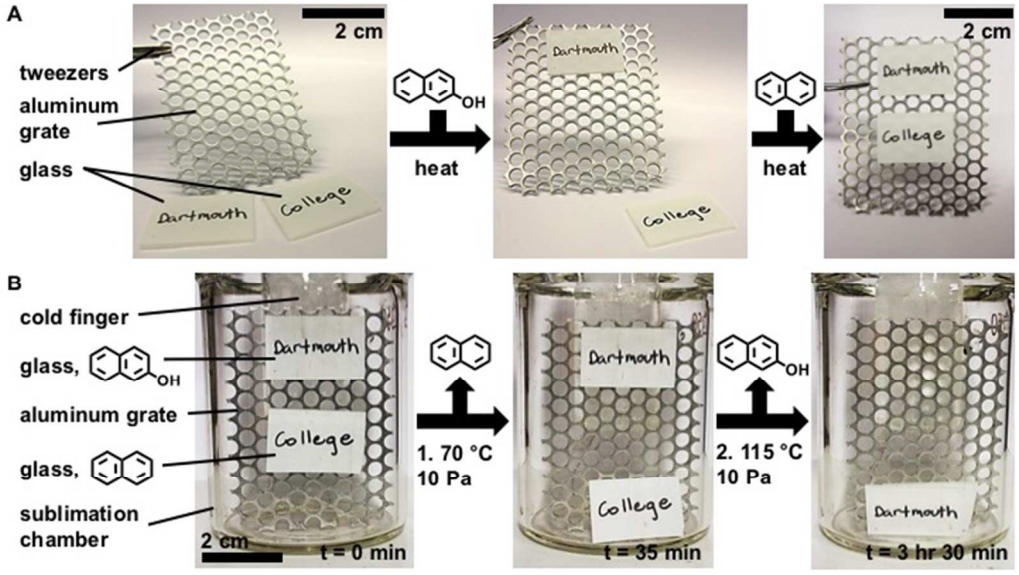

Figure S43. Sequential bonding and release of the two substrates, Dartmouth and College. A) Sequential bonding of glass substrate labeled "Dartmouth" and "College" to an aluminum grate using a heat gun. B) Sequential release of two glass substrates bonded with $C_{10}H_8$ (top, "Dartmouth") and $C_{10}H_7OH$ (bottom, "College") from an aluminum carrier with staggered pores (with a diameter of 0.4 cm). Vacuum assisted sublimation of $C_{10}H_8$ at 70 °C released the bottom substrate, "College". Subsequent increase in temperature to 115 °C released the top substrate, "Dartmouth".

XIV. Plasma Cleaning of PAH Residue from Released Pieces of R1OH

Contact angle measurement indicated residual PAH remained on the released R1OH surfaces from the debonding experiment in **SI Section XII**. To remove this residue, released R1OH substrates were treated using a plasma cleaner (Harrick Plasma, Model PDC-32G). To assess the efficacy of this treatment, contact angles were measured and used as a metric of cleanliness for the R1OH substrates. Contact angles were measured before bonding, after release, and after being treated in plasma cleaner (**Figure S44**) for a single piece of R1OH (25 × 20 mm). Plasma cleaner treatment entailed setting the plasma cleaner to "Hi" RF (radiofrequency electromagnetic radiation) setting for two minutes. Contact angles were measured 24 hours after treatment by plasma cleaner. After R1OH-substrates were bonded and released as described in the **SI Section XII**, the contact angles were measured as described in **SI Section II.2**. This experiment was performed for $C_{10}H_8$ and $C_{10}F_8$.

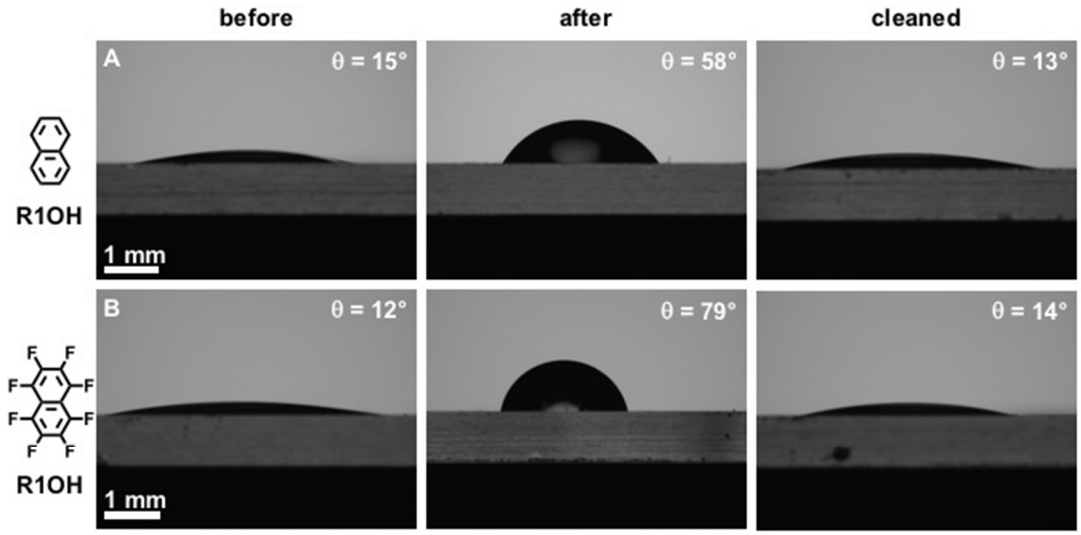

Figure S44. Using the contact angle (θ) of water on R1OH substrates to demonstrate the ability to remove PAH residue. A) Images of a water droplet (2 μL) on the same R1OH-substrate (20 × 25 × 1 mm) at three different stages; before melt-bonding to an aluminum carrier with $C_{10}H_8$, after releasing the substrate by sublimation, and after rapid plasma treatment. The contact angle of the water droplet is in the top, right corner of the image. B) Images of a water droplet (2 μL) on the same R1OH-substrate (20 × 25 × 1 mm) at three different stages: before melt-bonding to an aluminum carrier with $C_{10}F_8$, after releasing the substrate by sublimation, and after rapid plasma treatment. The contact angle of the water droplet is in the top, right corner of the image.

XV. Utility of Sublimable Adhesives in Mechanoelectronic Systems

1. Demonstration with One Switch and Two Lights in Mechanoelectronic System.

A circuit was built on a 5 × 5 cm circuit board (CB). Parts used for fabrication were connectors (3M, Jumper Wire Kit), one single-pole-double-throw (SPDT) switches (Honeywell Electronics), two resistors (560 ± 5% Ω (resistor$_G$) and 650 ± 5% Ω (resistor$_R$), Ohmite), two light emitting diodes (LEDs, a 3 mm red LED (LED$_R$) and 3 mm green LED (LED$_G$) purchased from Avago Technologies) a 23 mm coin cell holder (Memory Protection Devices), and 20 mm lithium-battery 3 V cell (Energizer Battery Company). **Figure S45A** and **S45B** show the circuit diagram and an image of a portion of the circuit. Its operation using PAHs as adhesives is illustrated in **Figure 4b**. The circuit was wired to have two LEDs and two resistors in parallel The LED$_R$ and LED$_G$ were wired to be in a closed circuit and open circuit, respectively, when the lever from the switch was not bonded to the bonding-post, also known as the "released" position (**Figure 4b**). When the lever is bonded to the bonding-post, known as the "adhered" position (**Figure 4b**), the LED$_R$ and LED$_G$ circuits change states to open and closed, respectively. The lever was bonded in the adhered state using $C_{10}H_8$. The components displayed in the **Figure S45A**, but not seen in **Figure S45B** are the R_R, R_G, coin cell holder, and connecting wiring.

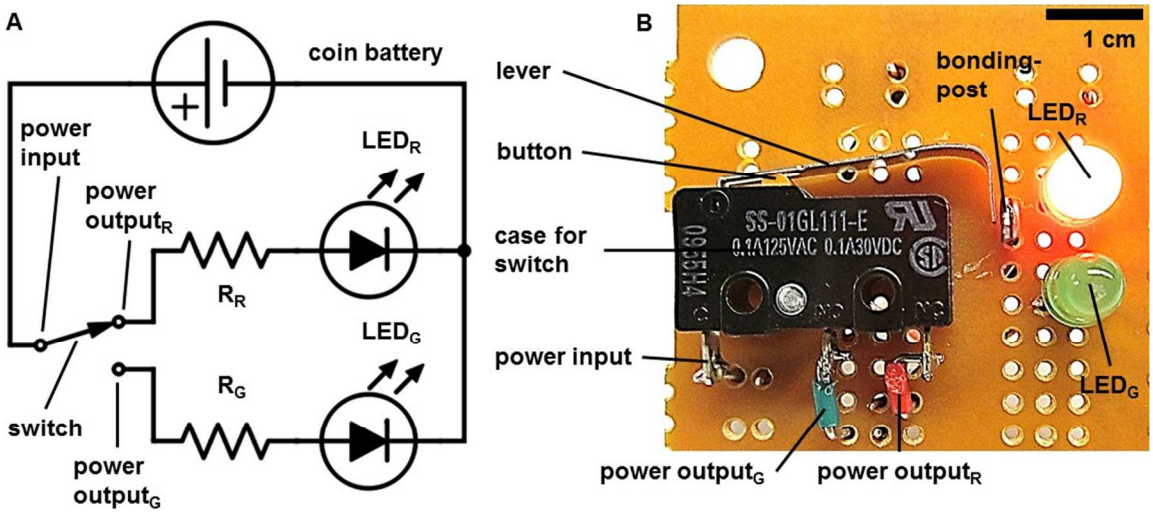

Figure S45. Circuit-diagram of mechanoelectronic system used in Figure 4b of the main text. A) A circuit diagram of components and wiring using standard notation for the mechanoelectronic system of **Figure 4b**. The circuit diagram was drawn in an online application called Scheme-It, provided by Digi-Key Electronics. B) The circuit depicted in **Figure S45A** was fabricated with components of interest on one side of the circuit board, shown above, and the remaining functional components (resistors and connecting wires) on the opposite side of the circuit board.

2. Expanded Demonstration of Utility of PAHs in Mechanoelectronic Systems. A circuit was built on an 11 × 4.75 cm CB. Parts used were connectors (3M, Jumper Wire Kit), three SPDT switches (Honeywell Electronics), three resistors (560 ± 5% Ω ($resistor_G$), 6.8 ± 5% kΩ ($resistor_R$), and 6.2 ± 5% kΩ ($resistor_Y$), Ohmite), three light emitting diodes (LEDs): green LED, (LED_G), red LED (LED_R), and yellow LED, (LED_Y), purchased from Avago Technologies, a 23 mm holder coin cell (Memory Protection Devices), and 20 mm lithium battery 3 V cell (Energizer Battery Company). **Figure S62** shows the circuit layout and its operation using PAHs as adhesives. The circuit was wired to have three sets of hinge-lever switches, resistors, and LEDs, in parallel. The LED_G and LED_Y were wired to be in an open circuit when the lever on the switch was released. The LED_R was wired to be in a closed circuit when the lever on the switch was adhered to the bonding-post. The levers for the LED_G and LED_Y were bonded in the "adhered state" using $C_{10}H_8$. The lever for the LED_R was bonded in the "adhered state" using $C_{10}H_7OH$. All components may be seen in the circuit diagram as well as optical micrograph of the mechanoelectronic system (**Figure S46A**).

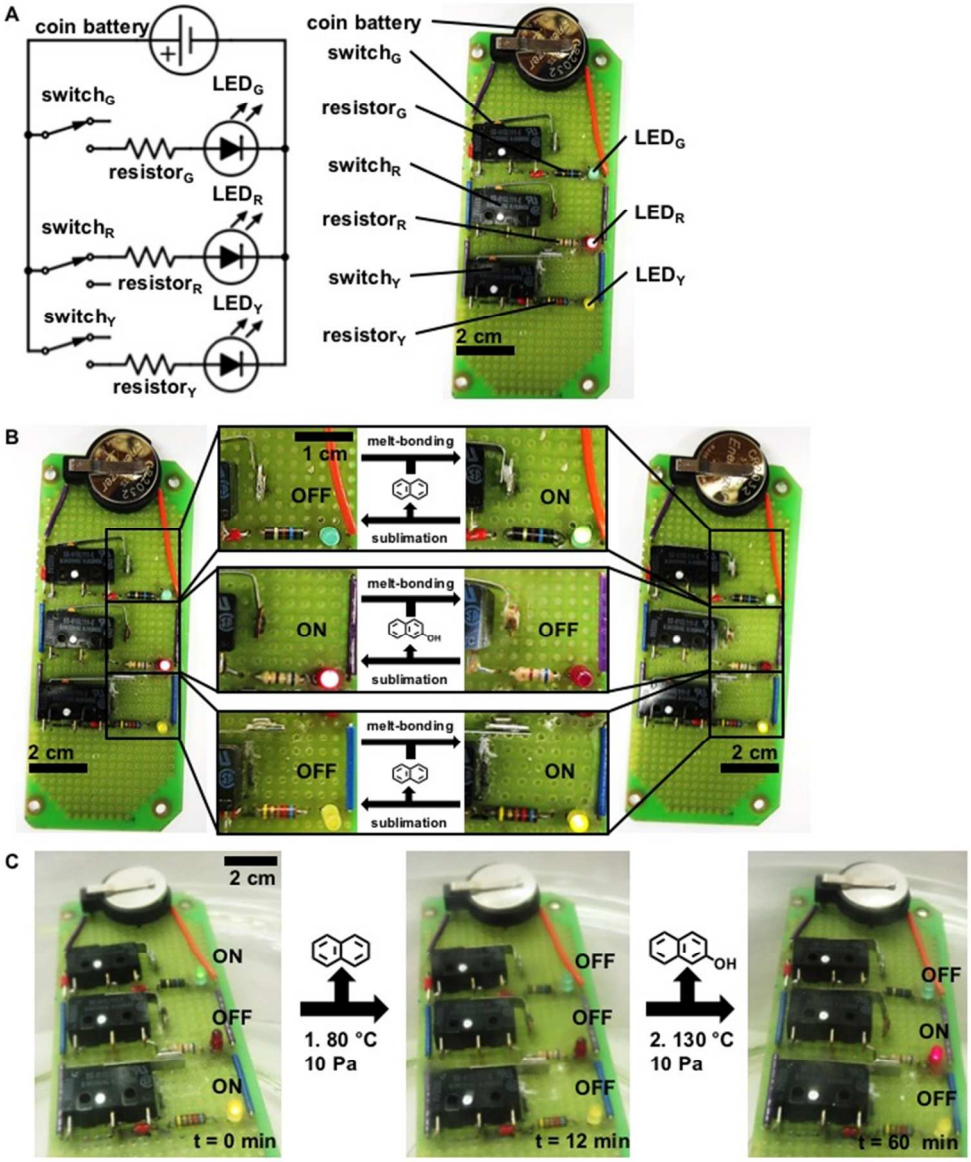

Figure S46. Using PAHs to sequentially release levers to switch LEDs ON or OFF. A) Schematic depiction and image of the circuit used to demonstrate the possibility for building complex systems using PAHs as adhesives. B) The levers of the circuit may be in the "released" and "adhered" state by melt-bonding or sublimation, respectively. C) Circuit functioning as designed in a large desiccator (repurposed as a sublimer) under 10 Pa and at two different temperatures, 80 °C and 130 °C, to remove two PAHs are distinctly different times.

XVI. Gaussian Calculations

The lowest energy structure of each PAH was optimized to full convergence with density functional theory (DFT) at the B3LYP/6-311++(3d,2p) level of theory in a gas phase model using Gaussian'09. Studies comparing levels of theory have demonstrated that DFT geometric optimization of PAHs display good agreement with experimental and/or accepted values at the B3LYP/6-311++(3d,2p) level of theory.[S30,S31] Our subsequent

$C_{10}H_8$ calculations matched reported results for $C_{10}H_8$,[S10] encouraging our claim of accurate relative comparisons between PAHs for the purposes of this study (**Table S13**). Electron density maps (at the same isosurface value) were visualized in GaussView5, and generated from electrostatic potentials computed through SCF electron density at the same level of theory utilized above (**Figure S47**).

Table S13. Theoretical potential energy and dipole moment calculated in Gaussian'09 confirms the polarity of $C_{10}H_6(OH)_2$ and $C_{10}H_6(NH_2)_2$. The overall energy (hartree) of the PAHs is reported and matches literature values. Overall dipole moment (debye) is reported for each scalar vector, x, y, and z, for $C_{10}H_8$, $C_{10}H_6(OH)_2$, $C_{10}H_6(NH_2)_2$, and $C_{10}F_8$.

Compound	Energy (hartree)	Dipole Moment (debye)			
		x	y	z	Overall
$C_{10}H_8$	-386.0032	0	0	0	0
$C_{10}H_6(OH)_2$	-536.5066	-0.5009	2.3187	0.0001	2.4338
$C_{10}H_6(NH_2)_2$	-496.7573	0.9970	-0.0878	0.6031	2.9702
$C_{10}F_8$	-1180.113	0	0	0	0

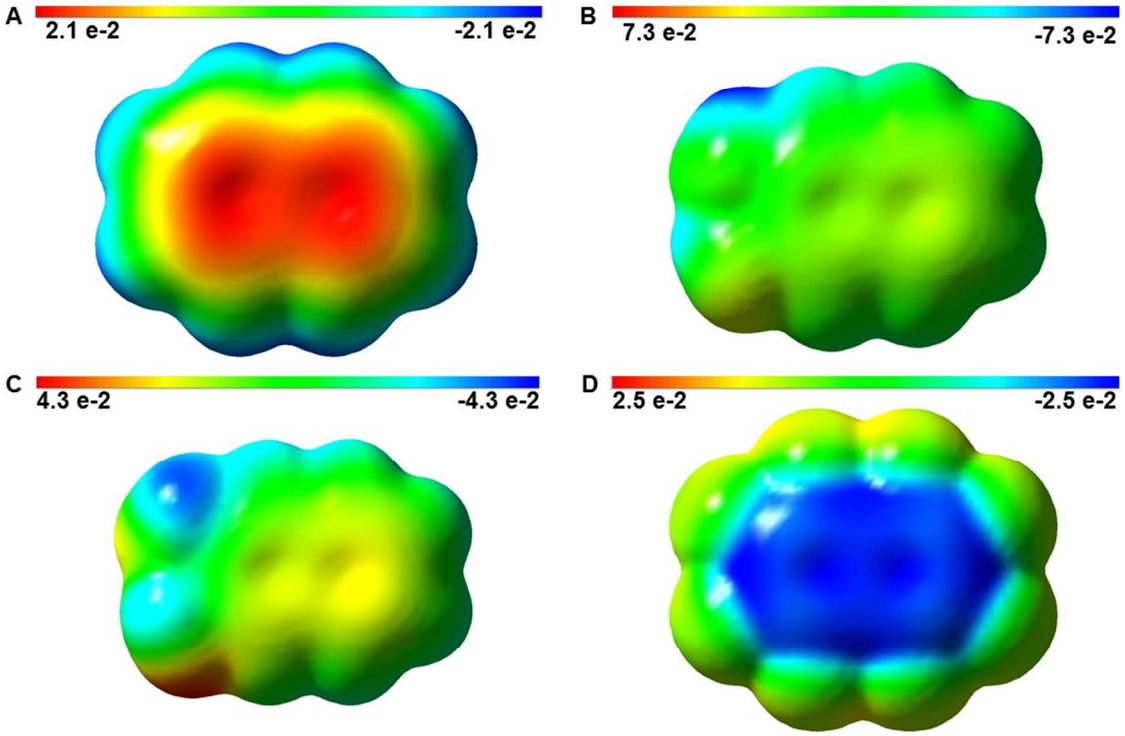

Figure S47. Electron density maps from total SCF density for A) $C_{10}H_8$, B) $C_{10}H_6(OH)_2$, C) $C_{10}H_6(NH_2)_2$, and D) $C_{10}F_8$.

Stationary Point Summaries: Stationary points were optimized as previously described and shown below. Atoms are given by atomic number, and geometries in Cartesian coordinates.

$C_{10}H_8$

Row	Symbol	X	Y	Z
1	C	2.4276420	0.7070200	0.0000020
2	C	1.2424570	1.3992410	-0.0000020
3	C	0.0000140	0.7149250	-0.0000010
4	C	-0.0000150	-0.7149200	-0.0000010
5	C	1.2424390	-1.3992410	-0.0000030
6	C	2.4276290	-0.7070390	0.0000020
7	H	-1.2412260	2.4816870	-0.0000060
8	H	3.3677550	1.2415480	0.0000030
9	H	1.2412550	2.4816780	0.0000000
10	C	-1.2424450	1.3992490	0.0000000
11	C	-1.2424600	-1.3992490	0.0000000
12	H	1.2412320	-2.4816810	0.0000010
13	H	3.3677380	-1.2415730	0.0000050
14	C	-2.4276370	-0.7070240	0.0000010
15	C	-2.4276250	0.7070360	0.0000020
16	H	-1.2412420	-2.4816830	-0.0000050
17	H	-3.3677630	-1.2415310	0.0000040
18	H	-3.3677630	-1.2415630	0.0000020

$C_{10}H_6(OH)_2$

Row	Symbol	X	Y	Z
1	C	3.1319940	0.7170950	-0.0000230
2	C	1.9412590	1.4029740	-0.0000280
3	C	0.7047180	0.7123900	-0.0000090
4	C	0.7092480	-0.7171470	0.0000100
5	C	1.9550580	-1.3932410	0.0000260
6	C	3.1383070	-0.6949530	0.0000150
7	H	-0.5575460	2.4745790	-0.0000110
8	H	4.0683810	1.2579270	-0.0000390
9	H	1.9356800	2.4855630	-0.0000570
10	C	-0.5417100	1.3908830	-0.0000150
11	C	-0.5259000	-1.4130220	0.0000350
12	H	1.9598460	-2.4755250	0.0000510
13	H	4.0800430	-1.2265070	0.0000260
14	C	-1.7151740	-0.7340610	0.0000060
15	C	-1.7154240	0.6884040	-0.0000110
16	H	-0.5410140	-2.4942420	0.0000640
17	O	-2.8976960	-1.4081980	-0.0000610
18	H	-3.6183490	-0.7669180	-0.0001640
19	O	-2.9673700	1.2550950	0.0000480
20	H	-2.9007660	2.2140190	0.0001980

$C_{10}H_6(NH_2)_2$

Row	Symbol	X	Y	Z
1	C	-5.2229440	1.5930620	1.2184590
2	C	-3.8534210	1.6931270	1.2233330
3	C	-3.0913450	1.5452240	0.0393370
4	C	-3.7734330	1.2720020	-1.1844710
5	C	-5.1869970	1.1928140	-1.1712020
6	C	-5.9092010	1.3585920	-0.0151350
7	H	-1.1610600	1.8460590	0.9561230
8	H	-3.3367170	1.8749730	2.1586700
9	C	-1.6786060	1.6406080	0.0272450
10	C	-3.0134020	1.1075570	-2.3678280
11	H	-5.7094290	1.0113200	-2.1034220
12	C	-1.6435760	1.2066890	-2.3473680
13	C	-0.9691300	1.4750880	-1.1371720
14	H	-3.5308750	0.9019710	-3.2967280
15	H	-1.0773540	1.0786670	-3.2602130
16	H	0.110035	1.5500700	-1.1295290
17	N	-7.3100560	1.2439240	0.0349400
18	H	-7.7467870	1.9572580	0.6037160
19	H	-7.7411280	1.2089350	-0.8763600
20	N	-6.0071120	1.7757770	2.3714030
21	H	-6.7568760	1.1017880	2.4528480
22	H	-5.4662150	1.8038500	3.2223470

$C_{10}F_8$

Row	Symbol	X	Y	Z
1	C	-2.4268160	-0.7031820	-0.0000420
2	C	-1.2447950	-1.3948970	-0.0002120
3	C	0.0000020	-0.7188490	-0.0001330
4	C	-0.0000100	0.7188430	0.0001400
5	C	-1.2447980	1.3949000	0.0003120
6	C	-2.4268260	0.7031880	0.0002220
7	C	1.2448130	-1.3948940	-0.0003100
8	C	1.2448020	1.3948880	0.0002190
9	C	2.4268170	0.7031930	0.0000380
10	C	2.4268300	-0.7031950	-0.0002310
11	F	3.5920060	1.3458740	0.0001080
12	F	3.5920150	-1.3458700	-0.0003990
13	F	1.2974140	-2.7287630	-0.0005530
14	F	-1.2974360	-2.7287630	-0.0004630
15	F	-3.5919980	-1.3458870	-0.0001200
16	F	-3.5920050	1.3458840	0.0003860
17	F	-1.2974120	2.7287590	0.0005620
18	F	1.2974040	2.7287680	0.0004760

XVII. Supporting References

M. J. Frisch, G. W. Trucks, H. B. Schlegel, G. E. Scuseria, M. A. Robb, J. R. Cheeseman, G. Scalmani, V. Barone, B. Mennucci, G. A. Petersson, H. Nakatsuji, M. Caricato, X. Li, H. P. Hratchian, A. F. Izmaylov, J. Bloino, G. Zheng, J. L. Sonnenberg, M. Hada, M. Ehara, K. Toyota, R. Fukuda, J. Hasegawa, M. Ishida, T. Nakajima, Y. Honda, O. Kitao, H. Nakai, T. Vreven, J. A. Montgomery Jr., J. E. Peralta, F. Ogliaro, M. Bearpark, J. J. Heyd, E. Brothers, K. N. Kudin, V. N. Staroverov, R. Kobayashi, J. Normand, K. Raghavachari, A. Rendell, J. C. Burant, S. S. Iyengar, J. Tomasi, M. Cossi, N. Rega, J. M. Millam, M. Klene, J. E. Knox, J. B. Cross, V. Bakken, C. Adamo, J. Jaramillo, R. Gomperts, R. E. Stratmann, O. Yazyev, A. J. Austin, R. Cammi, C. Pomelli, J. W. Ochterski, R. L. Martin, K. Morokuma, V. G. Zakrzewski, G. A. Voth, P. Salvador, J. J. Dannenberg, S. Dapprich, A. D. Daniels, Ö. Farkas, J. B. Foresman, J. V. Ortiz, J. Cioslowski, D. J. Fox, Gaussian 09 (Revision B.01), Gaussian, Inc., Wallingford, CT, 2009.

(S1) Bhushan, B. *Modern Tribology Handbook*, *Vol. 1*; CRC Press LLC: Boca Raton, **2000**.

(S2) Johns, I. B.; McElhill, E. A.; Smith, J. O. Thermal Stability of Some Organic Compounds. *J. Chem. Eng. Data* **1962**, *7*, 277-281.

(S3) Lial, M. L.; Hornsby, J.; Schneider, D.; Daniels, C. *Algebra and Trigonometry: Functions and Applications*; Prentice Hall: Upper Saddle River, NJ, **2005**.

(S4) References for density are listed in the following order, $C_{10}H_8$ (a), $C_{10}F_8$ (b), $C_{10}H_6(OH)_2$ (c), $C_{10}H_6(NH_2)_2$ (d), $C_{14}H_{10}$ (e), and $C_{16}H_{10}$ (f). a) Criterion and Standards Division, Office of Water Planning and Standards, U.S. Environmental Protection Agency, *Ambient Water Quality Criteria*; National Service Center for Environmental Protection: Washingtion, D.C., 2005; b) Guidechem, http://www.guidechem.com/dictionary/en/313-72-4.html, **2012**. Visited on August 18, 2016; c) Chemical Book, http://www.chemicalbook.com/ProductMSDSDetailCB8736136_EN.htm, **2016**. Visited on August 18, 2016; d) Santa Cruz Biotechnology, http://www.scbt.com/datasheet-202882-2-3-diaminonaphthalene.html, **2016**. Visited on August 18, 2016; e) O'Neil, M. J. *The Merck Index – An Encyclopedia of Chemicals, Drugs, and Biologicals*; Merck and Co.: Whitehouse Station, NJ, 2006; f) Lide, D. R. *CRC Handbook of Chemistry and Physics 88th Edition*; CRC Press: Taylor and Francis, Boca Raton, FL, **2007**.

(S5) *ASTM D-1002-10; Standard Test Method for Apparent Shear Strength of Single-Lap-Joint Adhesively Bonded Metal Specimens by Tension Loading (Metal-to-Metal);* ASTM International: West Conshohocken, PA, **2010**.

(S6) Hibbeler, R. C. *Mechanics of Materials*; Pearson Education: Upper Saddle River, NJ, **2004**.

(S7) Bourhis, E. L. *Glass: Mechanics and Technology*; Wiley-VCH: Weinheim, Germany, **2007**.

(S8) Ebewle, R. O. *Polymer Science and Technology*; CRC Press LLC: Boca Raton, FL, **2000**.

(S9) References for the pK_a-values for $C_{10}H_6(OH)_2$ (a), $C_{10}H_6(NH_2)_2$ (a), Si-OH (b), and acid-base chemistry in solid state materials (c). a) Perrin, D. D.; Dempsey, B.; Serjeant, E. P. *pK_a Prediction of Organic Acids and Bases*, *Chapter 5*; Springer: Berlin, Germany, **1981**; b) Liu, X.; Cheng, J.; Lu, X.; Wang, R. Surface acidity of quartz: understanding the crystallographic control. *Phys. Chem. Chem. Phys.* **2014**, *16*, 26909-26916; c) Li, Z. J.; Abramov, Y.; Bordner, J.; Leonard, J.; Medek, A.; Trask, A. V. Solid-State Acid-Base Interactions in Complexes of

Heterocyclic Bases with Dicarboxylic Acids: Crystallography, Hydrogen Bond Analysis, and 15N NMR Spectroscopy. *J. Am. Chem. Soc.* **2006**, *128*, 8199-8210.
(S10) References for the structure of mica (a) and the cleavage of single crystalline materials including mica (b). a) Pauling, L. The Structure of the Micas and Related Minerals. *Proc. Nat. Acad. Sci.* **1930**, *16*, 123-129; b) Schultz, R. A., Jensen, M. C., Bradt, R. C. Single Crystal Cleavage of Brittle Materials. *Int. J. Fract.* **1994**, *65*, 291-312.
(S11) Cheng, Y. J.; Yang, S. H.; Hsu, C. S. Synthesis of Conjugated Polymers for Organic Solar Cell Applications. *Chem. Rev.* **2009**, *109*, 5868-5923.
(S12) Pecharsky, V. K.; Zavaliji, R. Y. *Fundamentals of Powder Diffraction and Structural Characterization of Materials*; Springer: New York, **2009**.
(S13) Vazquez-Molina, D. A.; Mohammad-Pour, G. S.; Lee, C.; Logan, M. W.; Duan, X.; Harper J. K.; Uribe-Romo, F, J. Mechanically Shaped Two-Dimensional Covalent Organic Frameworks Reveal Crystallographic Alignment and Fast Li-Ion Conductivity. *J. Am. Chem. Soc.* **2016**, *138*, 9767-9770.
(S14) Oddershede, J.; Larsen, S. Charge Density Study of Naphthalene Based on X-ray Diffraction Data at Four Different Temperatures and Theoretical Calculations. *J. Phys. Chem. A* **2004**, *108*, 1057-1063.
(S15) Bel'skii, V. K.; Kharchenko, E. V.; Sobolev, A. N.; Zavodnik, V. E.; Kolomiets, N. A.; Prober, G. S.; Oleksenko, L. P. Crystal and Molecular Structure of Dihydroxynaphthalene Isomers. Effect of Structure on Ice-Forming Properties. *J. Struct. Chem.* **1991**, *31*, 791-795.
(S16) Bagryanskaya, I. Y.; Gatilov, Y. V.; Lork, E.; Mews, R.; Shakirov, M. M.; Watson, P. G.; Zibarev, Z. V. Molecular Complexes of Octafluoronaphthalene with Acyclic and Heterocyclic Sulfur–Nitrogen Compounds. *Fluorine Chem.* **2002**, *116*, 149-156.
(S17) Zhan, Y.; Barton, R. J.; Robertson, B. E. Structure of 2,3-Naphthalenedi-amine Di-hydrochloride Dehydrate. *Acta Cryst.* **1993**, *C49*, 46-48.
(S18) Hedlund, J.; Mintova, S.; Sterte, J. Controlling the Preferred Orientation in Silicalite-1 Films Synthesized by Seeding. *J. Micropor. Mesopor. Mat.* **1999**, *28*, 185-194.
(S19) McQuarrie, D. A.; Simon, J. D. *Physical Chemistry: A Molecular Approach*; University Science Books: Herndon, VA, **1997**.
(S20) Joback, K. G.; Reid, R. C. Estimation of Pure-Component Properties from Group-Contributions. *Chem. Eng. Commun.* **1987**, *57*, 233-243.
(S21) Rojas, A.; Orozco, E. Measurement of the Enthalpies of Vaporization and Sublimation of Solids Aromatic Hydrocarbons by Differential Scanning Calorimetry. *Thermochim. Acta.* **2003**, *405*, 93-107.
(S22) Khimeche, K.; Dahmani, A. Solid−Liquid Equilibria of Naphthalene + Alkanediamine Mixtures. *J. Chem. Eng. Data.* **2006**, *51*, 382-385.
(S23) Michaud, F.; Negrier, P.; Mikailitchen, D.; Oonk, H. A. J. Measurement and Analysis of the Naphthalene — Octafluoronaphthalene Phase Diagram: Complex Formation in Solid and Liquid. *Mol. Cryst. Liq. Crys. A.* **1999**, *326*, 409-424.
(S24) Storoniak, P.; Krymiński, K.; Bożyk, A.; Koval'chuk, E. P.; Blażejowski, J. Melting, Volatilisation and Crystal Lattice Enthalpies of Acridin-9(10H)-ones. *J. Therm. Anal. Calorim.* **2003**, *74*, 443-450.
(S25) Goldfarb, J. L.; Külaots, I. Melting Points and Enthalpies of Fusion of Anthracene and its Heteroatomic Counterparts. *J. Therm. Anal. Calorim.* **2010**, *102*, 1063-1070.
(S26) Torres-Gómez, L. A.; Barreiro-Rodríguez, G.; Galarza-Mondragón, A. A New Method for the Measurement of Enthalpies of Sublimation using Differential Scanning Calorimetry. *Thermochim. Acta.* **1988**, *124*, 229-233.

(S27) Stephenson, M. R.; Malanowski, S. *Handbook of the Thermodynamics of Organic Compounds*; Springer: Netherlands, **1987**.
(S28) Chickos, J. S.; Acree, W. E. Enthalpies of Sublimation of Organic and Organometallic Compounds. 1910–2001. *J. Phys. Chem. Ref. Data* **2002**, *31*, 537-698.
(S29) Goldfarb, L. J.; Suuberg, E. M. Vapor Pressures and Thermodynamics of Oxygen-Containing Polycyclic Aromatic Hydrocarbons Measured Using Knudsen Effusion. *Environ. Toxicol. Chem.* **2008**, *27*, 1244-1249.
(S30) Hinchliffe, A.; Nikolaidi, B.; Soscún, H. J. M. Density Functional Studies of the Dipole Polarizabilities of Substituted Stilbene, Azoarene and Related Push-Pull Molecules. *Int. J. Mol. Sci.* **2004**, *5*, 224-238.
(S31) Hinchliffe, A.; Perez, J. J.; Soscún, H. J. M. Density Functional Studies of Molecular Polarizabilities. Part 4: the $C_{10}H_8$ Molecules Azulene, Fulvalene and Naphthalene *Electron. J. Theor. Ch.* **1997**, *2*, 325-336.